fractal and fractional

MDPI

Article

Mathematical Modeling of Alzheimer's Drug Donepezil Hydrochloride Transport to the Brain after Oral Administration

Corina S. Drapaca

Department of Engineering Science and Mechanics, Pennsylvania State University, University Park, PA 16802, USA; csd12@psu.edu

Abstract: Alzheimer's disease (AD) is a progressive degenerative disorder that causes behavioral changes, cognitive decline, and memory loss. Currently, AD is incurable, and the few available medicines may, at best, improve symptoms or slow down AD progression. One main challenge in drug delivery to the brain is the presence of the blood–brain barrier (BBB), a semi-permeable layer around cerebral capillaries controlling the influx of blood-borne particles into the brain. In this paper, a mathematical model of drug transport to the brain is proposed that incorporates two mechanisms of BBB crossing: transcytosis and diffusion. To account for the structural damage and accumulation of harmful waste in the brain caused by AD, the diffusion is assumed to be anomalous and is modeled using spatial Riemann–Liouville fractional-order derivatives. The model's parameters are taken from published experimental observations of the delivery to mice brains of the orally administered AD drug donepezil hydrochloride. Numerical simulations suggest that drug delivery modalities should depend on the BBB fitness and anomalous diffusion and be tailored to AD severity. These results may inspire novel brain-targeted drug carriers for improved AD therapies.

Keywords: fractional derivatives; anomalous diffusion; BBB transcytosis; Alzheimer's disease; donepezil

Citation: Drapaca, C.S. Mathematical Modeling of Alzheimer's Drug Donepezil Hydrochloride Transport to the Brain after Oral Administration. *Fractal Fract.* **2024**, *8*, 496. https://doi.org/10.3390/fractalfract8090496

Academic Editors: Ivanka Stamova, Carla M. A. Pinto and Dana Copot

Received: 26 July 2024
Revised: 17 August 2024
Accepted: 20 August 2024
Published: 23 August 2024

1. Introduction

Alzheimer's disease (AD) is a multifactorial degenerative disorder of the cerebral neuro-glial-vascular units characterized by various progressive pathological factors such as the aggregation of amyloid-β ($A\beta$) plaques, the accumulation of tau-containing neurofibrillary tangles, and increases in neuroinflammation [1]. It is estimated that tens of millions of adults worldwide have AD and millions of new cases are added annually [2]. Currently, AD has no cure, and the few available medicines may, at best, improve symptoms or slow down AD progression.

Mechanisms of AD onset and progression continue to elude us more than a century after the first description of the disease was published [3]. One possible cause of AD is a substantial loss of cells in the neocortex, amygdala, and hippocampus that leads to a cholinergic deficit manifested as an inability to send neuronal messages across cholinergic synapses that eventually results in cognitive and functional dysfunctions. Another cause of AD may be the accumulation of neurofibrillary tangles. The excessive phosphorylation–dephosphorylation of tau, a protein that stabilizes microtubules (these structures maintain the complex neuronal morphologies), causes the removal of tau from the microtubules followed by the collapse of microtubules, the loss of neuronal functionality, the aggregation of the hyperphosphorylated tau (ptau) in neurofibrillary tangles, and, ultimately, neuronal apoptosis [1]. An abnormal division of the amyloid precursor protein (APP), a protein involved in cell health and growth, produces $A\beta$ monomers prone to aggregation into toxic $A\beta$ plaques that can also cause AD. The toxicity of the plaques damages the glymphatic pathway and the blood–brain barrier (BBB), which are involved in brain waste clearance [4,5]. This results in increased neuroinflammation, neurodegeneration, and, ultimately, death. Chronic inflammation in the brain is yet another possible cause of AD [6].

Sustained activation of microglia cells and astrocytes can cause neurodegeneration and facilitate the aggregation of $A\beta$ plaques and neurofibrillary tangles. The complex interlinks among these plausible AD causes explain the difficulty in finding effective AD therapies.

One treatment challenge is the BBB, a semi-permeable membrane shared by the sealed capillary endothelium surrounded by pericytes, perivascular astrocyte endfeet (from a structural point of view, it is unclear whether the astrocyte endfeet are part of the basement membrane [4] or linked to the membrane via protein binding [7]), and various junctional complexes (Figure 1) [4,7]. A functional BBB protects the brain parenchyma from harmful agents by tightly controlling the influx of most particles, including drugs, from blood to the brain. However, AD causes the disintegration of the BBB, which leads, among other effects, to the accumulation of neurotoxins in the brain, loss of diffusion and interstitial fluid (ISF) flow within the brain extracellular space (ECS), increased inflammatory and immune responses in the brain, and, ultimately, neurodegeneration and escalated AD progression [4,8,9]. These observations suggest that multi (BBB and brain)-targeted drug delivery and releasing modalities [1,4] that are tailored to AD severity may provide more effective AD therapies.

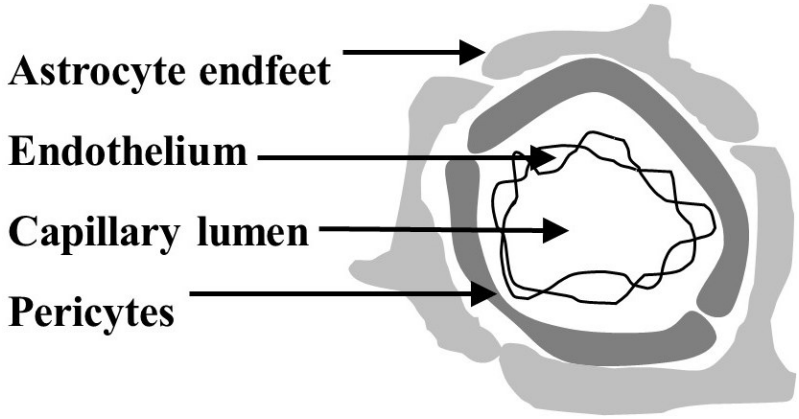

Figure 1. Schematic of the BBB structure: a basement membrane shared by endothelial cells, pericytes (immersed or chemically linked), astrocyte endfeet, and junctional complexes located at the interfaces of these cells (inspired by [4,7]).

Successful therapies for AD could use the BBB functions to safely deliver drugs to the brain and, at the same time, preserve/recover the structural integrity and functionality of the BBB. Possible mechanisms of BBB crossing that have been studied intensively for drug delivery to the brain are [4,7,10,11] transcytosis, efflux, paracellular transport, carrier-mediated transport, and diffusion. These mechanisms depend on the structures and chemical compositions of the BBB elements that control the transport of molecules and ions through various highly specialized biochemical interactions. Small lipophilic molecules, O_2, and CO_2 cross the BBB by simple diffusion [4,11]. Small hydrophilic molecules and ions can passively travel across the BBB via the paracellular pathway. Ions can also use specialized ion channels and pumps to traverse the BBB. Solutes use carrier-mediated transport for BBB crossing based on substrate specificity and concentration gradient. Efflux transporters strictly control the entry of most drugs and their conjugates into the brain. Transcytosis transports molecules across the BBB from the blood to the brain using vesicles [10]. The molecules are first internalized by vesicles by the endothelial cells at the lumen–endothelium interface, circulate inside the vesicles along different pathways inside the cells, and then are released on the other side of the cells to continue their transport to the brain parenchyma. The internalization may be adsorptive for electrostatically charged molecules or mediated by certain receptors for specific molecules. Toxic $A\beta$ species and some neurotoxins can be cleared by receptor-mediated transcytosis. Lastly, aquaporin (AQP) receptors (AQP1 on the endothelial cells and AQP4 on the perivascular astrocyte's endfeet) facilitate water transport through the BBB [4]. Also, AQP4 contributes to the

clearance of $A\beta$ and tau species from the brain via the glymphatic pathway [5,12]. Recent advancements in nanotechnology and the manufacturing of multifunctional biomaterials have facilitated the use of BBB transcytosis, among others, for pharmacological purposes.

Donepezil hydrochloride, a reversible acetylcholinesterase inhibitor, is one of the few FDA-approved drugs for treating mild, moderate, and severe AD [13]. The enzyme acetylcholinesterase disintegrates acetylcholine, a neurotransmitter released by neurons that facilitates communications among neurons [14]. Acetylcholine binds the neuronal nicotinic (cholinergic) receptors, which are the ligand-gated ion channels of neurons. By binding to acetylcholinesterase, donepezil increases the amount of acetylcholine available at the synapses for proper message transmissions. Additionally, a recent study [15] showed that donepezil was able to reduce the $A\beta$-induced microglial and astrocytic activation and thus decrease neuroinflammation in an AD mouse model. The drug may alleviate some symptoms of AD and, as the disease progresses, its dosage must be gradually increased. The combination between the AD progression and dosage increase worsens the gastrointestinal and heart-related adverse effects of the drug. Various delivery and releasing systems for donepezil that aim to reduce the side effects while preserving the drug's efficacy exist in the literature. For instance, mango gum polymeric donepezil-loaded nanoparticles were found to be nontoxic, and the intravenous injections of these nanoparticles in rats showed that the drug was successfully delivered to the brain [16]. In [17], extracellular vesicles isolated from human plasma were loaded with donepezil and injected intravenously into zebrafish. The study showed that the proposed drug formulation was nontoxic and had a better pharmacological response and reduced side effects. Donepezil-loaded systems like solid lipid nanoparticles with or without ApoE [18,19], cholesterol-modified pullulan nanoparticles with polysorbate 80 surface coverage [20], ternary sodium alginate-based hydrogels [21], lyotropic liquid crystalline mesophases composed of monoolein/oleic acid/water [22], and sodium alginate microspheres [23] exhibit desirable pharmacological features such as the ability to cross the BBB and nontoxic prolonged drug release. Lastly, nasal [24–26], subcutaneous [27], and transdermal [28] administrations of donepezil show comparable or better pharmacological responses than oral administration of the drug.

Mathematical modeling can help not only with advancing the knowledge of mechanisms of health and disease specific to the human body but also with designing drug delivery and release systems for successful therapies. Mathematical models with applications in pharmacology and medicine that exist in the literature belong to three distinct groups: (1) models of multiphysics processes taking place in the human body and happening at various spatio-temporal scales, (2) pharmacokinetic models of drug transport in the human body, and (3) models of drug release processes that depend on the drug formulations and delivery systems. Models of drug release are the most used in pharmacology since they can be easily fitted to experimental data [29–31]. Some of the most popular models of drug release (like Fick's, Higuchi's, Peppas', Hopfenberg's, and Weibull's models) predict cumulative drug release over time. Specifically, the Ritger–Peppas model describes both Fickian and non-Fickian temporal release behaviors of a drug from swelling or non-swelling materials and it was used in experimental studies of donepezil release (see, for instance, [23]). Pharmacokinetic models are compartmental (population) models describing mostly temporal variations and dynamic interactions among the drug concentrations corresponding to the bodily structures (compartments) the drug passes through. These models are represented mathematically as systems of ordinary differential equations with short (first-order temporal derivative) or long (fractional-order temporal derivative) memory [32–34]. Specifically, compartmental models were fitted to experimental observations of orally and nasally administrated donepezil in [24]. Mathematical models that link models of AD from all three modeling groups mentioned above do not exist yet.

Published models of drug delivery, release, and transport to a brain with AD focus only on the temporal dynamics of the drug's concentration and ignore specific structural and biophysical aspects of the brain and the spatial variations in the drug's concentration. These models have limited practical utility since the success of AD therapies depends on the ability

of brain-targeted drug delivery systems to accurately deliver drugs to specific brain regions of interest. Models that can predict spatio-temporal variations in a drug concentration during transport to the brain are more helpful in developing brain-targeted drug delivery systems. In this paper, a mathematical model of AD drug donepezil hydrochloride transport to the brain after oral administration is proposed that incorporates specific structural and biophysical aspects of the BBB and brain parenchyma in the presence of AD. The model generalizes the pharmacokinetic model described in [24] by including spatial variations of donepezil in a blood–brain region and in the presence of (1) the BBB transcytosis and (2) anomalous diffusion due to the structural damage and accumulation of harmful waste in the brain caused by AD. The anomalous diffusion is modeled as Lévy flights with index $\varepsilon + 1$, $0 < \varepsilon < 1$ and is represented mathematically by spatial Riemann–Liouville fractional derivatives of order ε. It is assumed that functional BBB transcytosis corresponds to an earlier stage of AD, while the absence of BBB transcytosis (due to the BBB disintegration) represents a later stage of AD, and both of these scenarios are investigated. Numerical simulations show that both functional BBB transcytosis and anomalous diffusion are essential for increasing the concentration of donepezil in the brain parenchyma. The results suggest that it is not an increase in the donepezil dosage and/or frequency but rather different drug delivery and release modalities dependent on the AD severity that may help with treatment effectiveness during AD progression. An original schematic for a multi (BBB and brain)-targeted drug delivery system is also presented that suggests using ligands of various lengths and binding affinities attached to the donepezil molecules to practically realize Lévy jumps. This study may inspire new brain-targeted drug nanocarriers for improved AD therapies.

This paper is organized as follows. The mathematical model and corresponding numerical discretization are presented in Section 2. The results and numerical simulations are shown in Section 3. In Section 4, a discussion of the presented work and its potential usages is given. The paper ends with a brief conclusion in Section 5.

2. Mathematical Modeling

2.1. Model Formulation

A compartmental model that accounts for temporal and spatial variations in donepezil's concentration is proposed. The two compartments are a depot and a combined blood–brain region. The depot is a region in the body where the drug is stored and from which it is slowly distributed; for orally administered drugs, the depot is the stomach. The combined blood–brain region is a micron-sized region within the cerebral capillary bed. The geometric domain of the model is shown in Figure 2. It is made of concentric horizontal axial symmetric circular cylinders of length L representing a capillary lumen of radius a_0, a BBB of thickness d_{BBB}, and a layer of thickness $d - d_{BBB}$ filled with brain parenchyma made of ECS, neurons, and glial cells. Due to the chosen geometry and axial symmetry, cylindrical coordinates are used: $(r, z) \in [0,\, a_0 + d] \times [0,\, L]$.

Let $C_d : \mathrm{S} \times [0,\, T] \to \mathbf{R}^+$ and $C : [0,\, a_0 + d] \times [0,\, L] \times [0,\, T] \to \mathbf{R}^+$ be the concentrations of the drug in the depot and in the coupled blood–brain region, respectively, depicted in Figure 2. The concentrations are assumed to be absolutely continuous functions, which implies the temporal differentiability almost everywhere on $[0,\, T]$ of C_d and C [35] and the existence of spatial left- and right-sided Riemann–Liouville fractional derivatives of order $0 < \varepsilon < 1$ almost everywhere on $[0,\, a_0 + d]$ and $[0,\, L]$ of C [36]. Since in this model the only role of the concentration C_d is to contribute to the production of the concentration C in the capillary lumen, a mathematical descripton of the physical depot is irrelevant and, thus, without loss of generality, the spatial domain of C_d can be taken to be $\mathrm{S} = [0,\, a_0 + d] \times [0,\, L]$.

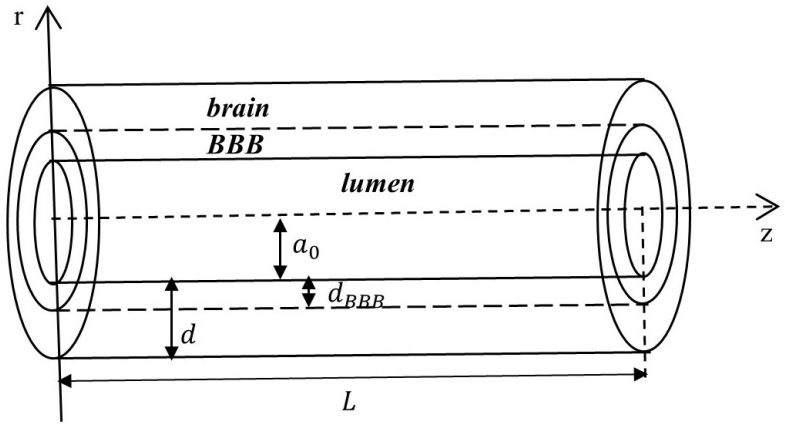

Figure 2. The geometric domain is made of concentric horizontal axial symmetric circular cylinders of length L representing a capillary lumen of radius a_0, a BBB of thickness d_{BBB}, and a region of thickness $d - d_{BBB}$ filled with brain parenchyma.

The balance law of mass gives

$$\frac{\partial C_d(r,z,t)}{\partial t} = -k_{12}\, t^{\alpha}\, C_d(r,z,t), \tag{1}$$

$$\begin{aligned}\frac{\partial C(r,z,t)}{\partial t} &= -\frac{1}{r}\frac{\partial}{\partial r}(r\, F_1(r,z,t)) - \frac{\partial}{\partial z}F_2(r,z,t)\\ &+ (k_{12}\, t^{\alpha}\, C_d(r,z,t) - k_{20}\, C(r,z,t))[1 - H(r-a_0)]\\ &- k_{23}\, C(a_0,z,t)[H(r-(a_0-\beta)) - H(r-a_0)]\\ &+ V_{\text{blood}}/V_{\text{brain}}\, k_{23}\, C(a_0,z,t)[H(r-(a_0+d_{BBB}-\beta)) - H(r-(a_0+d_{BBB}))]\\ &- k_{30}\, C(r,z,t)[H(r-(a_0+d_{BBB})) - H(r-(a_0+d))].\end{aligned} \tag{2}$$

Above, H denotes the Heaviside step function approximated by the following smooth function [37]: $H(r) = \frac{1}{\pi}\left(\frac{3\pi}{4} + \arctan(r-1) + \arctan\left(\frac{2-r}{r}\right)\right)$, $r > 0$. Also, the capillary lumen–BBB and BBB–brain interfaces are modeled as thin layers (while, from a strictly structural point of view, the capillary lumen–BBB and BBB–brain interfaces could be seen as crisp boundaries, the BBB-specific biochemical processes may happen in a region wider than the BBB and, thus, these interfaces may look more like fuzzy boundaries) of thickness β where the preparations for the starting and ending of BBB-specific biochemical processes occur. Drug's advection is neglected since AD causes both a dramatic reduction in cerebral blood flow and capillary stalling [38,39] and the loss of ISF flow through the extracellular space [4].

The two-dimensional diffusion flux (F_1, F_2) is given by the generalized Fick's law describing anomalous diffusion (see, for instance, [40]):

$$\begin{aligned}F_1(r,z,t) &= -D\left[p_r\, \partial^{\varepsilon_r}_{L_{r+}} C(r,z,t) - q_r\, \partial^{\varepsilon_r}_{R_{r-}} C(r,z,t)\right],\\ F_2(r,z,t) &= -D\left[p_z\, \partial^{\varepsilon_z}_{L_{z+}} C(r,z,t) - q_z\, \partial^{\varepsilon_z}_{R_{z-}} C(r,z,t)\right],\end{aligned} \tag{3}$$

where D is a generalized diffusion coefficient, $0 < \varepsilon_r, \varepsilon_z \leq 1$ are parameters related to radial and longitudinal long-range interactions of drug particles, and $p_r, q_r, p_z, q_z \geq 0$ are probabilities of moving in the outward/forward and, respectively, inward/backward diffusional radial/longitudinal directions. These probabilities satisfy the constraints $p_r + q_r = 1$, $p_z + q_z = 1$. For now, it is assumed that $\varepsilon_r = \varepsilon_z = \varepsilon$. The left- and right-sided Riemann–Liouville fractional derivatives of order ε with $0 < \varepsilon \leq 1$ are, by definition [36],

$$\partial^{\varepsilon}_{L_{r+}} C(r,z,t) = \frac{1}{\Gamma(1-\varepsilon)} \frac{\partial}{\partial r} \int_{L_r}^{r} \frac{C(\widetilde{r},z,t)}{(r-\widetilde{r})^{\varepsilon}} d\widetilde{r},\ \partial^{\varepsilon}_{L_{z+}} C(r,z,t) = \frac{1}{\Gamma(1-\varepsilon)} \frac{\partial}{\partial z} \int_{L_z}^{z} \frac{C(r,\widetilde{z},t)}{(z-\widetilde{z})^{\varepsilon}} d\widetilde{z},$$
$$\partial^{\varepsilon}_{R_{r-}} C(r,z,t) = \frac{1}{\Gamma(1-\varepsilon)} \frac{\partial}{\partial r} \int_{r}^{R_r} \frac{C(\widetilde{r},z,t)}{(\widetilde{r}-r)^{\varepsilon}} d\widetilde{r},\ \partial^{\varepsilon}_{R_{z-}} C(r,z,t) = \frac{1}{\Gamma(1-\varepsilon)} \frac{\partial}{\partial z} \int_{z}^{R_z} \frac{C(r,\widetilde{z},t)}{(\widetilde{z}-z)^{\varepsilon}} d\widetilde{z}, \quad (4)$$

where $\Gamma(s) = \int_0^{\infty} \tau^{s-1} \mathrm{e}^{\tau} d\tau$ is the gamma function, $L_r = L_z = 0$, $R_r = a_0 + d$, and $R_z = L$. If $\varepsilon = 1$ and $p_r = p_z = 0.5$, then Formula (3) becomes the classic Fick's law.

Since the model applies to the AD drug donepezil hydrochloride, the sinks and sources in Equations (1) and (2) are adapted from [24] and [23]. For simplicity, the notations of the parameters taken from [24] are kept the same here. In Equation (2), the term containing parameter k_{12} represents the drug's absorption through the depot to the blood, while parameter k_{20} is an elimination rate due to biochemical processes taking place within the capillary lumen. The unidirectional BBB transcytosis is modeled as sinks along the capillary lumen–BBB interface and sources along the BBB–brain interface that are proportional to $C(a_0, z, t)$. The drug's transfer rate at the sinks is k_{23}, while at the sources it has to be rescaled since the volume of drug distribution (the volume of distribution in a body's region is the amount of the drug in that region divided by the plasma concentration) in the brain, V_{brain}, is different from the volume of distribution in the blood, V_{blood} [24]. Lastly, parameter k_{30} represents the elimination rate of the drug from the brain (occupying the region $(r,z) \in (a_0 + d_{BBB}, a_0 + d) \times (0, L)$) due to various brain-specific biochemical processes. Lastly, the term t^{α} is added to both Equations (1) and (2) to model the oral administration of either a drug solution [24] for $\alpha = 0$ or donepezil-encapsulated sodium alginate microspheres with controlled drug release according to a power law function [23] for $\alpha \in [0.5, 1)$.

A model of more severe BBB damage could be obtained by removing the terms representing the BBB transcytosis from Equation (2) and thus expanding the region occupied by the brain parenchyma to $(r,z) \in (a_0, a_0 + d) \times (0, L)$:

$$\begin{aligned} \frac{\partial C(r,z,t)}{\partial t} &= -\frac{1}{r}\frac{\partial}{\partial r}(r\, F_1(r,z,t)) - \frac{\partial}{\partial z} F_2(r,z,t) \\ &+ (k_{12}\, t^{\alpha}\, C_d(r,z,t) - k_{20}\, C(r,z,t))[1 - H(r-a_0)] \\ &- k_{30}\, C(r,z,t)[H(r-a_0) - H(r-(a_0+d))]. \end{aligned} \quad (5)$$

The systems of Equations (1) and (2), and, respectively, (1) and (5) are solved numerically using the following boundary and initial conditions:

$$\begin{aligned} C_d(0,z,t) = C_d(a_0+d,z,t) = 0,\ C_d(r,0,t) = C_d(r,L,t) = 0, \\ C(0,z,t) = C(a_0+d,z,t) = 0,\ C(r,0,t) = C(r,L,t) = 0, \\ C_d(r,z,0) = 0.8961 \times [1 - H(r-a_0)]\left[1 - \frac{z}{L}\right],\ C(r,z,0) = 0. \end{aligned} \quad (6)$$

The initial condition for C_d in (6) is estimated from [24].

Noting that Equation (1) is a first-order separable and linear ordinary differential equation with respect to the variable t, its closed-form solution ca be easily found to be

$$C_d(r,z,t) = C_d(r,z,0)\, \mathrm{e}^{-\frac{k_{12}}{\alpha+1} t^{\alpha+1}},\ (r,z) \in (0, a_0+d) \times (0,L). \quad (7)$$

Figure 3 shows plots of the initial condition $C_d(r,z,0)$ and solution (7) at fixed location (r, z). As the value of α increases, the concentration C_d decreases faster to zero with time (Figure 3b).

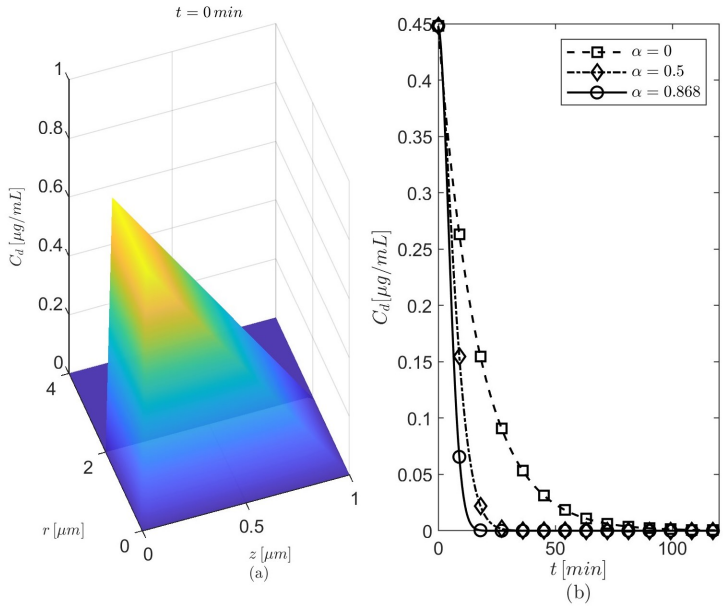

Figure 3. (**a**) Plot of the initial condition $C_d(r, z, 0)$ given by Formula (6). (**b**) Temporal variation in C_d at location $r = 0.96$ µm, $z = 0.5$ µm calculated using Formula (7) for various values of α.

Semi-analytic solutions of Equations (2) and (5) may be found by using the Laplace and Fourier transforms and series representations likely combined with some numerical algorithms. However, this is not the solution approach used here. In this paper, Equations (2) and (5) are solved numerically using MATLAB R2024a [41].

2.2. Numerical Discretization

Inserting Formula (3) into the first two terms of the right hand side of Equation (2) (or (5)) and using the fact that

$$\frac{\partial}{\partial r}\left(\partial^{\varepsilon}_{L_{r+}} C\right) = \partial^{\varepsilon+1}_{L_{r+}} C,\ \frac{\partial}{\partial z}\left(\partial^{\varepsilon}_{L_{z+}} C\right) = \partial^{\varepsilon+1}_{L_{z+}} C,$$
$$\frac{\partial}{\partial r}\left(\partial^{\varepsilon}_{R_{r-}} C\right) = -\partial^{\varepsilon+1}_{R_{r-}} C,\ \frac{\partial}{\partial z}\left(\partial^{\varepsilon}_{R_{z-}} C\right) = -\partial^{\varepsilon+1}_{R_{z-}} C$$

gives

$$-\frac{1}{r}\frac{\partial}{\partial r}(r\,F_1) - \frac{\partial}{\partial z}F_2 = \frac{D}{r}\left(p_r \partial^{\varepsilon}_{L_{r+}} C - q_r \partial^{\varepsilon}_{R_{r-}} C\right) + D\left(p_r \partial^{\varepsilon+1}_{L_{r+}} C + q_r \partial^{\varepsilon+1}_{R_{r-}} C + p_z \partial^{\varepsilon+1}_{L_{z+}} C + q_z \partial^{\varepsilon+1}_{R_{z-}} C\right). \quad (8)$$

Grünwald–Letnikov formulas [42] are used to numerically discretize the left- and right-sided Riemann–Liouville fractional-order derivatives. Let $L_r = 0 = r_0 < r_1 < ... < r_{N-1} < r_N = a_0 + d = R_r$ and $L_z = 0 = z_0 < z_1 < ... < z_{M-1} < z_M = L = R_z$ be equally spaced discretizations of the intervals $[0,\ a_0 + d]$ and, respectively, $[0,\ L]$ of constant step sizes $\Delta r = (a_0 + d)/N,\ \Delta z = L/M$. At every point $(r_k,\ z_l),\ k \in \{1, 2, ..., N-1\}$, $z \in \{1, 2, ..., M-1\}$, the following approximations are replaced in Formula (8):

$$\partial^{\varepsilon}_{L_{r+}} C(r_k, z_l, t) = \frac{1}{\Delta r^{\varepsilon}} \sum_{j=1}^{N-1} a_{jk} C(r_j, z_l, t), \quad \partial^{\varepsilon}_{R_{r-}} C(r_k, z_l, t) = \frac{1}{\Delta r^{\varepsilon}} \sum_{j=1}^{N-1} a_{kj} C(r_j, z_l, t),$$

$$\partial^{\varepsilon+1}_{L_{r+}} C(r_k, z_l, t) = \frac{1}{\Delta r^{\varepsilon+1}} \sum_{j=1}^{N-1} b_{jk} C(r_j, z_l, t), \quad \partial^{\varepsilon+1}_{R_{r-}} C(r_k, z_l, t) = \frac{1}{\Delta r^{\varepsilon+1}} \sum_{j=1}^{N-1} b_{kj} C(r_j, z_l, t),$$

$$\partial^{\varepsilon+1}_{L_{z+}} C(r_k, z_l, t) = \frac{1}{\Delta z^{\varepsilon+1}} \sum_{j=1}^{M-1} \tilde{b}_{jl} C(r_k, z_j, t), \quad \partial^{\varepsilon+1}_{R_{z-}} C(r_k, z_l, t) = \frac{1}{\Delta z^{\varepsilon+1}} \sum_{j=1}^{M-1} \tilde{b}_{lj} C(r_k, z_j, t), \quad (9)$$

where

$$a_{jk} = \begin{cases} g^{\varepsilon}_{k-j}, & j \le k \\ 0, & otherwise \end{cases}, \quad b_{jk} = \begin{cases} g^{\varepsilon+1}_{k-j+1}, & j \le k+1 \\ 0, & otherwise \end{cases}, \quad \tilde{b}_{jl} = \begin{cases} \tilde{g}^{\varepsilon+1}_{l-j+1}, & j \le l+1 \\ 0, & otherwise \end{cases}$$

with

$$g^{\varepsilon}_k = \frac{(-1)^k \Gamma(\varepsilon+1)}{\Gamma(k+1)\Gamma(\varepsilon-k+1)}, \; g^{\varepsilon+1}_k = \frac{(-1)^k \Gamma(\varepsilon+2)}{\Gamma(k+1)\Gamma(\varepsilon-k+2)}, \; k \in \{0, 1, ..., N\}$$

and $\tilde{g}^{\varepsilon+1}_l = \frac{(-1)^l \Gamma(\varepsilon+2)}{\Gamma(l+1)\Gamma(\varepsilon-l+2)}$, $l \in \{0, 1, ..., M\}$.

Note that numerical scheme (9) at a point (r_k, z_l) does not involve only the adjacent points of (r_k, z_l) but also farther away points, which highlights the non-locality of the Riemann–Liouville fractional-order derivatives.

Inserting Formula (9) into expression (8) and then inserting this discrete form of expression (8) into Equation (2) yields a system of ordinary differential equations that is solved numerically using MATLAB's built-in function **ode15s** with the non-negative option selected since negative values of the concentration C are unphysical. A similar approach is also used to numerically solve Equation (5).

3. Results

The values of the model's geometry and parameters used in numerical simulations are given in Table 1. The typical wall thickness of a brain capillary for mice was measured post mortem using synchrotron radiation-based micro computed tomography and is about 0.3 µm [43]. Since the capillary's endothelium is part of the BBB (see Figure 1), the thickness of the BBB is then taken to be $d_{BBB} = 0.5$ µm. The time period is $T = 300$ min and the step sizes of the numerical discretization are $\Delta r = 0.08$, $\Delta z = 0.025$, and $\Delta t = 0.6$ (a justification for the chosen step sizes is given at the end of this section). The thickess of the lumen–BBB and BBB–brain interfaces is $\beta = \Delta r$. Based on the differences among the temporal profiles of C_d seen in Figure 3b, results are presented for $\alpha = 0$ and $\alpha = 0.868$. The anomalous diffusion is investigated using either $p_r = p_z = 0.5$ (the probability for particles to move outward/forward is the same as that for particles to move inward/backward in the radial/longitudinal directions) or $p_r = 1$, $p_z = 0.5$ (the particles have a stronger movement in the outward radial direction). The radially outward skewness may enhance the amount of donepezil diffused into the brain parenchyma. The values of $\max_{t \in [0,T]} C(r, z, t)$ at various fixed points (r, z) and several values of ε, p_r, and p_z, either in the absence or in the presence of the BBB transcytosis and for the two chosen values of α, are presented in Tables 2–5. Due to space limitations, only some relevant cases from these tables are shown in Figures 4–11.

Table 1. The values and physical units of the model's geometry and parameters.

Considerations	Parameters	Values and Units [Reference]
Geometry	a_0	2 μm [43]
	d	2 μm
	d_{BBB}	0.5 μm
	L	1 μm
Physics	k_{12}	$0.059\,\text{min}^{-\alpha-1}$ [24]
	k_{20}	$0.012\,\text{min}^{-1}$ [24]
	k_{23}	$0.014\,\text{min}^{-1}$ [24]
	k_{30}	$0.325\,\text{min}^{-1}$ [24]
	V_{blood}	279 mL [24]
	V_{brain}	18 mL [24]
	D	$0.006\,\mu\text{m}^{\varepsilon+1}\cdot\text{min}^{-1}$ [23]
	α	{0, 0.868} [23,24]
	ε	{0.25, 0.5, 0.658, 0.868, 1}
	p_r, p_z	{0.5, 1}

Table 2. The values of $\max_{t\in[0,T]} C(r,z,t)$ at various locations (r,z) in the brain parenchyma for $\alpha = 0$ and several values of ε, p_r, and p_z, in the absence of the BBB transcytosis (C is solution to Equation (5)).

Case	r	$z = 0.25\,\mu$m	$z = 0.5\,\mu$m	$z = 0.75\,\mu$m
$\varepsilon = 1$, $p_r = p_z = 0.5$	2.56 μm	3.70×10^{-4} μg/mL	4.59×10^{-4} μg/mL	2.90×10^{-4} μg/mL
	2.8 μm	5.07×10^{-5} μg/mL	6.58×10^{-5} μg/mL	4.30×10^{-5} μg/mL
	3.04 μm	7.07×10^{-6} μg/mL	9.45×10^{-6} μg/mL	6.34×10^{-6} μg/mL
$\varepsilon = 0.868$, $p_r = p_z = 0.5$	2.56 μm	5.63×10^{-4} μg/mL	6.21×10^{-4} μg/mL	3.76×10^{-4} μg/mL
	2.8 μm	1.90×10^{-4} μg/mL	2.08×10^{-4} μg/mL	1.26×10^{-4} μg/mL
	3.04 μm	9.42×10^{-5} μg/mL	1.01×10^{-4} μg/mL	6.12×10^{-5} μg/mL
$\varepsilon = 0.658$, $p_r = p_z = 0.5$	2.56 μm	7.93×10^{-4} μg/mL	7.47×10^{-4} μg/mL	4.29×10^{-4} μg/mL
	2.8 μm	3.76×10^{-4} μg/mL	3.53×10^{-4} μg/mL	2.03×10^{-4} μg/mL
	3.04 μm	2.18×10^{-4} μg/mL	2.05×10^{-4} μg/mL	1.18×10^{-4} μg/mL
$\varepsilon = 0.5$, $p_r = p_z = 0.5$	2.56 μm	8.38×10^{-4} μg/mL	7.06×10^{-4} μg/mL	3.91×10^{-4} μg/mL
	2.8 μm	4.38×10^{-4} μg/mL	3.70×10^{-4} μg/mL	2.06×10^{-4} μg/mL
	3.04 μm	2.67×10^{-4} μg/mL	2.27×10^{-4} μg/mL	1.26×10^{-4} μg/mL
$\varepsilon = 0.25$, $p_r = p_z = 0.5$	2.56 μm	5.72×10^{-4} μg/mL	4.16×10^{-4} μg/mL	2.19×10^{-4} μg/mL
	2.8 μm	3.24×10^{-4} μg/mL	2.36×10^{-4} μg/mL	1.24×10^{-4} μg/mL
	3.04 μm	2.07×10^{-4} μg/mL	1.51×10^{-4} μg/mL	7.97×10^{-5} μg/mL
$\varepsilon = 0.868$, $p_r = 1$, $p_z = 0.5$	2.56 μm	8.35×10^{-4} μg/mL	8.96×10^{-4} μg/mL	5.36×10^{-4} μg/mL
	2.8 μm	3.44×10^{-4} μg/mL	3.69×10^{-4} μg/mL	2.21×10^{-4} μg/mL
	3.04 μm	1.83×10^{-4} μg/mL	1.96×10^{-4} μg/mL	1.17×10^{-4} μg/mL
$\varepsilon = 0.658$, $p_r = 1$, $p_z = 0.5$	2.56 μm	1.35×10^{-3} μg/mL	1.24×10^{-3} μg/mL	7.06×10^{-4} μg/mL
	2.8 μm	6.97×10^{-4} μg/mL	6.48×10^{-4} μg/mL	3.71×10^{-4} μg/mL
	3.04 μm	4.19×10^{-4} μg/mL	3.92×10^{-4} μg/mL	2.25×10^{-4} μg/mL
$\varepsilon = 0.5$, $p_r = 1$, $p_z = 0.5$	2.56 μm	1.45×10^{-3} μg/mL	1.20×10^{-3} μg/mL	6.59×10^{-4} μg/mL
	2.8 μm	8.06×10^{-4} μg/mL	6.75×10^{-4} μg/mL	3.73×10^{-4} μg/mL
	3.04 μm	5.08×10^{-4} μg/mL	4.28×10^{-4} μg/mL	2.37×10^{-4} μg/mL
$\varepsilon = 0.25$, $p_r = 1$, $p_z = 0.5$	2.56 μm	9.88×10^{-4} μg/mL	7.11×10^{-4} μg/mL	3.72×10^{-4} μg/mL
	2.8 μm	5.88×10^{-4} μg/mL	4.26×10^{-4} μg/mL	2.23×10^{-4} μg/mL
	3.04 μm	3.88×10^{-4} μg/mL	2.81×10^{-4} μg/mL	1.48×10^{-4} μg/mL

Assuming that the AD treatment has a better outcome when donepezil is able to reach neurons located in close proximity to the BBB [44,45], the maximum drug's concentrations at neuronal locations near the BBB are more relevant to the design of neuronal drug delivery

systems than the average or maximum concentration in the brain region. At this initial stage, the maximum concentrations of donepezil at arbitrarily chosen locations in the brain parenchyma near the BBB are calculated. By analyzing the data in Tables 2–5, the following observations can be made.

Table 3. The values of $\max_{t\in[0,T]} C(r,z,t)$ at various locations (r,z) in the brain parenchyma for $\alpha = 0$ and several values of ε, p_r, and p_z in the presence of BBB transcytosis (C is the solution to Equation (2)).

Case	r	$z = 0.25\,\mu m$	$z = 0.5\,\mu m$	$z = 0.75\,\mu m$
$\varepsilon = 1$, $p_r = p_z = 0.5$	2.56 μm	1.31×10^{-2} μg/mL	1.68×10^{-2} μg/mL	1.10×10^{-2} μg/mL
	2.8 μm	1.82×10^{-3} μg/mL	2.42×10^{-3} μg/mL	1.62×10^{-3} μg/mL
	3.04 μm	2.57×10^{-4} μg/mL	3.50×10^{-4} μg/mL	2.38×10^{-4} μg/mL
$\varepsilon = 0.868$, $p_r = p_z = 0.5$	2.56 μm	1.56×10^{-2} μg/mL	1.92×10^{-2} μg/mL	1.26×10^{-2} μg/mL
	2.8 μm	1.95×10^{-3} μg/mL	2.47×10^{-3} μg/mL	1.65×10^{-3} μg/mL
	3.04 μm	3.61×10^{-4} μg/mL	4.57×10^{-4} μg/mL	3.05×10^{-4} μg/mL
$\varepsilon = 0.658$, $p_r = p_z = 0.5$	2.56 μm	2.09×10^{-2} μg/mL	2.35×10^{-2} μg/mL	1.51×10^{-2} μg/mL
	2.8 μm	2.00×10^{-3} μg/mL	2.31×10^{-3} μg/mL	1.50×10^{-3} μg/mL
	3.04 μm	5.04×10^{-4} μg/mL	5.65×10^{-4} μg/mL	3.61×10^{-4} μg/mL
$\varepsilon = 0.5$, $p_r = p_z = 0.5$	2.56 μm	2.60×10^{-2} μg/mL	2.71×10^{-2} μg/mL	1.69×10^{-2} μg/mL
	2.8 μm	1.87×10^{-3} μg/mL	1.96×10^{-3} μg/mL	1.23×10^{-3} μg/mL
	3.04 μm	5.56×10^{-4} μg/mL	5.60×10^{-4} μg/mL	3.45×10^{-4} μg/mL
$\varepsilon = 0.25$, $p_r = p_z = 0.5$	2.56 μm	3.74×10^{-2} μg/mL	3.28×10^{-2} μg/mL	1.90×10^{-2} μg/mL
	2.8 μm	1.27×10^{-3} μg/mL	1.12×10^{-3} μg/mL	6.50×10^{-4} μg/mL
	3.04 μm	4.37×10^{-4} μg/mL	3.70×10^{-4} μg/mL	2.11×10^{-4} μg/mL
$\varepsilon = 0.868$, $p_r = 1$, $p_z = 0.5$	2.56 μm	1.38×10^{-2} μg/mL	1.69×10^{-2} μg/mL	1.10×10^{-2} μg/mL
	2.8 μm	1.93×10^{-3} μg/mL	2.41×10^{-3} μg/mL	1.60×10^{-3} μg/mL
	3.04 μm	4.81×10^{-4} μg/mL	5.96×10^{-4} μg/mL	3.92×10^{-4} μg/mL
$\varepsilon = 0.658$, $p_r = 1$, $p_z = 0.5$	2.56 μm	1.38×10^{-2} μg/mL	1.54×10^{-2} μg/mL	9.87×10^{-3} μg/mL
	2.8 μm	2.03×10^{-3} μg/mL	2.27×10^{-3} μg/mL	1.45×10^{-3} μg/mL
	3.04 μm	7.66×10^{-4} μg/mL	8.26×10^{-4} μg/mL	5.19×10^{-4} μg/mL
$\varepsilon = 0.5$, $p_r = 1$, $p_z = 0.5$	2.56 μm	1.21×10^{-2} μg/mL	1.25×10^{-2} μg/mL	7.82×10^{-3} μg/mL
	2.8 μm	1.90×10^{-3} μg/mL	1.91×10^{-3} μg/mL	1.18×10^{-3} μg/mL
	3.04 μm	8.33×10^{-4} μg/mL	8.04×10^{-4} μg/mL	4.85×10^{-4} μg/mL
$\varepsilon = 0.25$, $p_r = 1$, $p_z = 0.5$	2.56 μm	5.94×10^{-3} μg/mL	5.79×10^{-3} μg/mL	3.83×10^{-3} μg/mL
	2.8 μm	1.09×10^{-3} μg/mL	9.10×10^{-4} μg/mL	5.48×10^{-4} μg/mL
	3.04 μm	5.51×10^{-4} μg/mL	4.36×10^{-4} μg/mL	2.43×10^{-4} μg/mL

We observe the following for $\alpha = 0$:

- The largest amounts of donepezil at all the locations considered in the brain parenchyma are achieved for $\varepsilon = 0.5$, $p_r = 1$, and $p_z = 0.5$ in the absence of the BBB transcytosis and for $\varepsilon = 0.868$, and $p_r = p_z = 0.5$ when the BBB transcytosis is present;
- The concentrations C at all locations in the brain parenchyma are higher when the BBB transcytosis happens than when the BBB transcytosis is absent for each of the considered combinations of values of ε, p_r, and p_z;
- In the absence of the BBB transcytosis, the concentrations of the drug are higher at all locations in the brain parenchyma when the radial skewness $p_r = 1$ is considered than when it is not ($p_r = 0.5$) for each value of $\varepsilon < 1$ and fixed $p_z = 0.5$;
- When the BBB transcytosis is present, the radial skewness $p_r = 1$ does not provide any advantage over the case $p_r = 0.5$.

We observe the following for $\alpha = 0.868$:

- The largest amounts of donepezil at all the locations considered in the brain parenchyma are achieved for $\varepsilon = 0.5$, $p_r = 1$, and $p_z = 0.5$ (comparable values to those for

$\varepsilon = 0.658$, $p_r = 1$, and $p_z = 0.5$) in the absence of the BBB transcytosis and for $\varepsilon = 1$ and $p_r = p_z = 0.5$ when the BBB transcytosis is present;

- The concentrations C at all locations in the brain parenchyma are higher when the BBB transcytosis happens than when the BBB transcytosis is absent for each of the considered combinations of values of ε, p_r, and p_z;
- In the absence of the BBB transcytosis, the concentrations of the drug are higher at all locations in the brain parenchyma when the radial skewness $p_r = 1$ is considered than when it is not ($p_r = 0.5$) for each value of $\varepsilon < 1$ and fixed $p_z = 0.5$;
- When the BBB transcytosis is present, the radial skewness $p_r = 1$ does not provide any advantage over the case $p_r = 0.5$.

The maximum concentrations for the case where $\alpha = 0.868$ are bigger than the corresponding values for the case where $\alpha = 0$.

Based on these findings, only the following cases are chosen to show their corresponding spatio-temporal variations in the drug's concentrations: $\varepsilon = 1$, $p_r = p_z = 0.5$, $\alpha \in \{0, 0868\}$ (Figures 4 and 5), $\varepsilon = 0.868$, $p_r = p_z = 0.5$, $\alpha \in \{0, 0868\}$ (Figures 6 and 7), $\varepsilon = 0.5$, $p_r = p_z = 0.5$, $\alpha \in \{0, 0868\}$ (Figures 8 and 9), and $\varepsilon = 0.5$, $p_r = 1$, $p_z = 0.5$, $\alpha \in \{0, 0868\}$ (Figures 10 and 11).

Table 4. The values of $\max_{t\in[0,T]} C(r,z,t)$ at various locations (r,z) in the brain parenchyma for $\alpha = 0.868$ and several values of ε, p_r, and p_z, in the absence of the BBB transcytosis (C is the solution to Equation (5)).

Case	r	$z = 0.25\,\mu m$	$z = 0.5\,\mu m$	$z = 0.75\,\mu m$
$\varepsilon = 1$, $p_r = p_z = 0.5$	2.56 μm	7.34×10^{-4} μg/mL	8.94×10^{-4} μg/mL	5.54×10^{-4} μg/mL
	2.8 μm	9.68×10^{-5} μg/mL	1.24×10^{-4} μg/mL	8.05×10^{-5} μg/mL
	3.04 μm	1.31×10^{-5} μg/mL	1.74×10^{-5} μg/mL	1.16×10^{-5} μg/mL
$\varepsilon = 0.868$, $p_r = p_z = 0.5$	2.56 μm	1.06×10^{-3} μg/mL	1.13×10^{-3} μg/mL	6.63×10^{-4} μg/mL
	2.8 μm	3.53×10^{-4} μg/mL	3.67×10^{-4} μg/mL	2.14×10^{-4} μg/mL
	3.04 μm	1.78×10^{-4} μg/mL	1.81×10^{-4} μg/mL	1.04×10^{-4} μg/mL
$\varepsilon = 0.658$, $p_r = p_z = 0.5$	2.56 μm	1.45×10^{-3} μg/mL	1.27×10^{-3} μg/mL	6.97×10^{-4} μg/mL
	2.8 μm	6.90×10^{-4} μg/mL	5.97×10^{-4} μg/mL	3.27×10^{-4} μg/mL
	3.04 μm	4.00×10^{-4} μg/mL	3.46×10^{-4} μg/mL	1.89×10^{-4} μg/mL
$\varepsilon = 0.5$, $p_r = p_z = 0.5$	2.56 μm	1.46×10^{-3} μg/mL	1.14×10^{-3} μg/mL	6.06×10^{-4} μg/mL
	2.8 μm	7.63×10^{-4} μg/mL	5.92×10^{-4} μg/mL	3.16×10^{-4} μg/mL
	3.04 μm	4.64×10^{-4} μg/mL	3.60×10^{-4} μg/mL	1.92×10^{-4} μg/mL
$\varepsilon = 0.25$, $p_r = p_z = 0.5$	2.56 μm	8.84×10^{-4} μg/mL	6.15×10^{-4} μg/mL	3.17×10^{-4} μg/mL
	2.8 μm	4.98×10^{-4} μg/mL	3.47×10^{-4} μg/mL	1.79×10^{-4} μg/mL
	3.04 μm	3.17×10^{-4} μg/mL	2.21×10^{-4} μg/mL	1.14×10^{-4} μg/mL
$\varepsilon = 0.868$, $p_r = 1$, $p_z = 0.5$	2.56 μm	1.61×10^{-3} μg/mL	1.65×10^{-3} μg/mL	9.49×10^{-4} μg/mL
	2.8 μm	6.57×10^{-4} μg/mL	6.66×10^{-4} μg/mL	3.83×10^{-4} μg/mL
	3.04 μm	3.51×10^{-4} μg/mL	3.53×10^{-4} μg/mL	2.02×10^{-4} μg/mL
$\varepsilon = 0.658$, $p_r = 1$, $p_z = 0.5$	2.56 μm	2.54×10^{-3} μg/mL	2.16×10^{-3} μg/mL	1.17×10^{-3} μg/mL
	2.8 μm	1.30×10^{-3} μg/mL	1.11×10^{-3} μg/mL	6.05×10^{-4} μg/mL
	3.04 μm	7.74×10^{-4} μg/mL	6.65×10^{-4} μg/mL	3.63×10^{-4} μg/mL
$\varepsilon = 0.5$, $p_r = 1$, $p_z = 0.5$	2.56 μm	2.59×10^{-3} μg/mL	1.98×10^{-3} μg/mL	1.05×10^{-3} μg/mL
	2.8 μm	1.43×10^{-3} μg/mL	1.10×10^{-3} μg/mL	5.83×10^{-4} μg/mL
	3.04 μm	8.89×10^{-4} μg/mL	6.87×10^{-4} μg/mL	3.65×10^{-4} μg/mL
$\varepsilon = 0.25$, $p_r = 1$, $p_z = 0.5$	2.56 μm	1.58×10^{-3} μg/mL	1.09×10^{-3} μg/mL	5.62×10^{-4} μg/mL
	2.8 μm	9.24×10^{-4} μg/mL	6.41×10^{-4} μg/mL	3.30×10^{-4} μg/mL
	3.04 μm	6.01×10^{-4} μg/mL	4.18×10^{-4} μg/mL	2.15×10^{-4} μg/mL

Table 5. The values of $\max_{t\in[0,T]} C(r,z,t)$ at various locations (r,z) in the brain parenchyma for $\alpha = 0.868$ and several values of ε, p_r, and p_z, in the presence of the BBB transcytosis (C is the solution to Equation (2)).

Case	r	$z = 0.25\,\mu m$	$z = 0.5\,\mu m$	$z = 0.75\,\mu m$
$\varepsilon = 1,\ p_r = p_z = 0.5$	2.56 μm	2.11×10^{-2} μg/mL	2.65×10^{-2} μg/mL	1.71×10^{-2} μg/mL
	2.8 μm	2.86×10^{-3} μg/mL	3.77×10^{-3} μg/mL	2.51×10^{-3} μg/mL
	3.04 μm	3.98×10^{-4} μg/mL	5.39×10^{-4} μg/mL	3.66×10^{-4} μg/mL
$\varepsilon = 0.868,\ p_r = p_z = 0.5$	2.56 μm	2.43×10^{-2} μg/mL	2.87×10^{-2} μg/mL	1.83×10^{-2} μg/mL
	2.8 μm	2.94×10^{-3} μg/mL	3.65×10^{-3} μg/mL	2.40×10^{-3} μg/mL
	3.04 μm	5.28×10^{-4} μg/mL	6.63×10^{-4} μg/mL	4.38×10^{-4} μg/mL
$\varepsilon = 0.658,\ p_r = p_z = 0.5$	2.56 μm	3.03×10^{-2} μg/mL	3.19×10^{-2} μg/mL	1.97×10^{-2} μg/mL
	2.8 μm	2.81×10^{-3} μg/mL	3.10×10^{-3} μg/mL	1.95×10^{-3} μg/mL
	3.04 μm	7.17×10^{-4} μg/mL	7.59×10^{-4} μg/mL	4.69×10^{-4} μg/mL
$\varepsilon = 0.5,\ p_r = p_z = 0.5$	2.56 μm	3.53×10^{-2} μg/mL	3.39×10^{-2} μg/mL	2.02×10^{-2} μg/mL
	2.8 μm	2.46×10^{-3} μg/mL	2.44×10^{-3} μg/mL	1.48×10^{-3} μg/mL
	3.04 μm	7.56×10^{-4} μg/mL	7.00×10^{-4} μg/mL	4.13×10^{-4} μg/mL
$\varepsilon = 0.25,\ p_r = p_z = 0.5$	2.56 μm	4.43×10^{-2} μg/mL	3.64×10^{-2} μg/mL	2.05×10^{-2} μg/mL
	2.8 μm	1.47×10^{-3} μg/mL	1.23×10^{-3} μg/mL	6.96×10^{-4} μg/mL
	3.04 μm	5.13×10^{-4} μg/mL	4.07×10^{-4} μg/mL	2.26×10^{-4} μg/mL
$\varepsilon = 0.868,\ p_r = 1,\ p_z = 0.5$	2.56 μm	2.17×10^{-2} μg/mL	2.54×10^{-2} μg/mL	1.61×10^{-2} μg/mL
	2.8 μm	2.94×10^{-3} μg/mL	3.59×10^{-3} μg/mL	2.33×10^{-3} μg/mL
	3.04 μm	7.27×10^{-4} μg/mL	8.78×10^{-4} μg/mL	5.67×10^{-4} μg/mL
$\varepsilon = 0.658,\ p_r = 1,\ p_z = 0.5$	2.56 μm	2.03×10^{-2} μg/mL	2.11×10^{-2} μg/mL	1.29×10^{-2} μg/mL
	2.8 μm	2.96×10^{-3} μg/mL	3.09×10^{-3} μg/mL	1.89×10^{-3} μg/mL
	3.04 μm	1.16×10^{-3} μg/mL	1.15×10^{-3} μg/mL	6.85×10^{-4} μg/mL
$\varepsilon = 0.5,\ p_r = 1,\ p_z = 0.5$	2.56 μm	1.65×10^{-2} μg/mL	1.56×10^{-2} μg/mL	9.24×10^{-3} μg/mL
	2.8 μm	2.62×10^{-3} μg/mL	2.40×10^{-3} μg/mL	1.40×10^{-3} μg/mL
	3.04 μm	1.21×10^{-3} μg/mL	1.04×10^{-3} μg/mL	5.92×10^{-4} μg/mL
$\varepsilon = 0.25,\ p_r = 1,\ p_z = 0.5$	2.56 μm	6.83×10^{-3} μg/mL	5.86×10^{-3} μg/mL	3.85×10^{-3} μg/mL
	2.8 μm	1.31×10^{-3} μg/mL	9.93×10^{-4} μg/mL	5.51×10^{-4} μg/mL
	3.04 μm	7.13×10^{-4} μg/mL	5.11×10^{-4} μg/mL	2.70×10^{-4} μg/mL

The spatial variations in the concentrations C at 30 min, 60 min, and 120 min after oral administration of donepezil in the absence of the BBB transcytosis have similar patterns for $\alpha = 0$ and $\varepsilon = 1$, $p_r = p_z = 0.5$ (Figure 4A(a–c)), $\varepsilon = 0.868$, $p_r = p_z = 0.5$ (Figure 6A(a–c)), $\varepsilon = 0.5$, $p_r = p_z = 0.5$ (Figure 8A(a–c)), and, respectively, for $\alpha = 0.868$ and $\varepsilon = 1$, $p_r = p_z = 0.5$ (Figure 4C(a–c)), $\varepsilon = 0.868$, $p_r = p_z = 0.5$ (Figure 6C(a–c)), $\varepsilon = 0.5$, $p_r = p_z = 0.5$ (Figure 8C(a–c)). As the time increases, the transport along the longitudinal direction is faster for $\alpha = 0.868$ (Figures 4C(a–c), 6C(a–c), and 8C(a–c)) than for $\alpha = 0$ (Figures 4A(a–c), 6A(a–c), and 8A(a–c)) for each of the combinations of the values of ε, p_r, and p_z mentioned above. Although the spatial variations in the concentrations C at 30 min, 60 min, and 120 min after oral administration of donepezil in the absence of the BBB transcytosis for $\varepsilon = 0.5$, $p_r = 1$, $p_z = 0.5$, shown in Figure 10A(a–c),C(a–c), look different from those discussed above, similar behavior is observed. The faster decline of C in the radial direction inside the capillary lumen is due to the radially outward skewness ($p_r = 1$, $q_r = 0$). On the other hand, the sharp decreases in time of the tempo-radial variations in the concentrations C at $z = 0.25\,\mu m$, $z = 0.5\,\mu m$, and $z = 0.75\,\mu m$ in the absence of the BBB transcytosis are similar for both cases $\alpha = 0$ and $\alpha = 0.868$ when $p_r = p_z = 0.5$ (Figures 4A(d–f),C(d–f), 6A(d–f),C(d–f), and 8A(d–f),C(d–f)). However, for $\varepsilon = 0.5$, $p_r = 1$, $p_z = 0.5$ the tempo-radial surfaces have sharp decreases in time and fast radial declines near the lumen center, followed by almost constant regions and then faster radial decreases near the lumen–brain interface, highlighting again the effect of the

radially outward skewness (Figure 10A(d–f),C(d–f)). Lastly, Figures 4B,D, 6B,D, 8B,D, and 10B,D show that in the presence of the BBB transcytosis, second hills appear inside the brain parenchyma near the BBB–brain interface that become higher at later times and with increasing values of z. Again, a faster decrease in drug concentration is observed for the case where $\alpha = 0.868$ than the case where $\alpha = 0$.

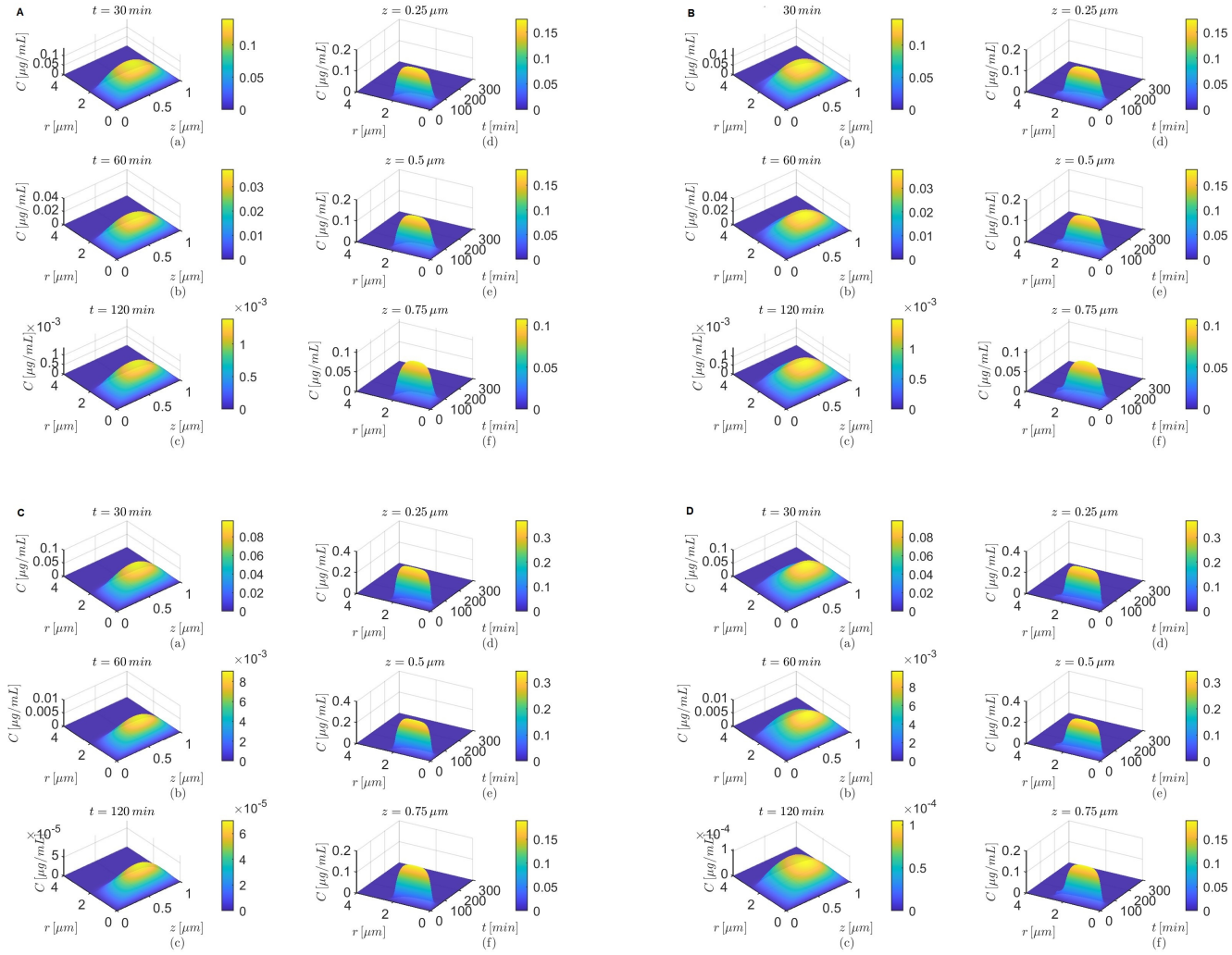

Figure 4. Results for $\varepsilon = 1$, $p_r = p_z = 0.5$, and $\alpha = 0$ (**A**,**B**) and $\alpha = 0.868$ (**C**,**D**) either in the absence (**A**,**C**) or in the presence (**B**,**D**) of the BBB transcytosis. Spatial variations in concentration C at three fixed times are shown in plots (**a–c**), and variations in C in time and along the radial direction at fixed locations along the capillary lumen are shown in plots (**d–f**).

Figures 5, 7, 9, and 11 show temporal variations in the concentration C at selected locations (r, z) in the lumen and, respectively, the brain parenchyma. The plots show that after it reaches a maximum the concentration C in the brain parenchyma decreases slower with time in the presence of the BBB transcytosis than when the BBB transcytosis is absent, and the decrease becomes slower as ε decreases. As expected (see Figure 3b), the shapes of the concentrations C in the brain parenchyma are narrower for the case where $\alpha = 0.868$ (Figures 5C,D, 7C,D, 9C,D, and 11C,D) than the case where $\alpha = 0$ (Figures 5A,B, 7A,B, 9A,B, and 11A,B) for each of the chosen combinations of the values of ε, p_r, and p_z regardless of whether the BBB transcytosis is present or not.

Lastly, for $\varepsilon = 1$, $p_r = p_z = 0.5$ the drug's concentration decreases fast inside the brain parenchyma away from the BBB–brain interface in both scenarios—the absence and the presence of BBB transcytosis (Figure 5A(d–f)–D(d–f)). However, for $\varepsilon < 1$ a more

gradual decrease in concentration is observed inside the brain parenchyma in the absence or the presence of the BBB transcytosis (Figures 7A(d–f)–D(d–f), 9A(d–f)–D(d–f), and 11A(d–f)–D(d–f)).

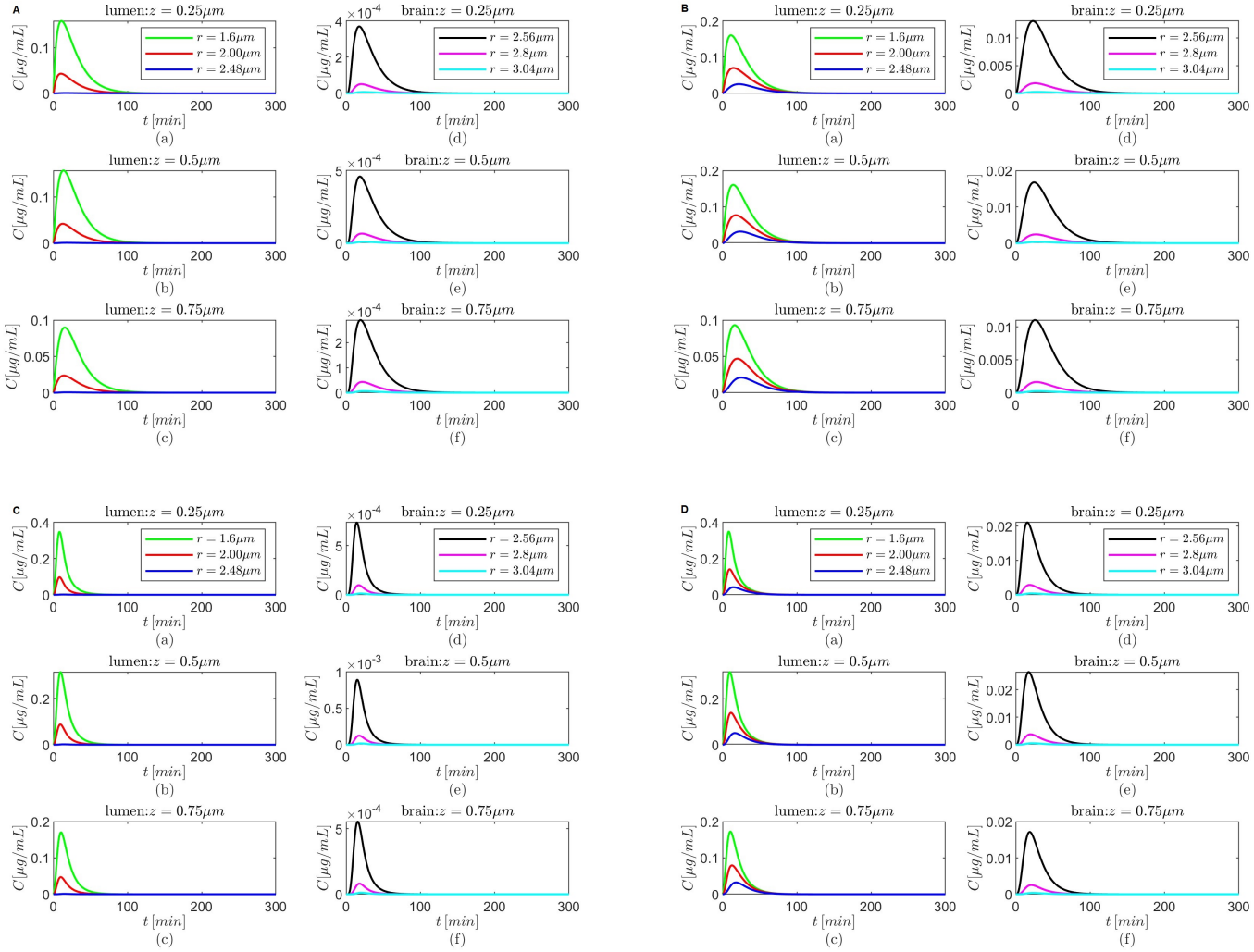

Figure 5. Results for $\varepsilon = 1$, $p_r = p_z = 0.5$, and $\alpha = 0$ (**A**,**B**) and $\alpha = 0.868$ (**C**,**D**) either in the absence (**A**,**C**) or in the presence (**B**,**D**) of the BBB transcytosis. Temporal variations in concentration C at various fixed locations in the capillary lumen (**a**–**c**) and brain parenchyma (**d**–**f**).

The convergence of the numerical scheme was also studied for the case where $\alpha = 0$, $\varepsilon = 0.868$, and $p_r = p_z = 0.5$ in the presence of the BBB transcytosis. The combined space–time convergence was investigated for the following step sizes: $S_1 = \{\Delta r = 0.16, \Delta z = 0.05, \Delta t = 1.2\}$, $S_{1/2} = \{\Delta r = 0.08, \Delta z = 0.025, \Delta t = 0.6\}$ and $S_{1/4} = \{\Delta r = 0.04, \Delta z = 0.0125, \Delta t = 0.3\}$, and the time step size convergence was studied for the fixed spatial step sizes $\Delta r = 0.08$, $\Delta z = 0.025$ and the time step sizes $\Delta t_1 = 1.2$, $\Delta t_{1/2} = 0.6$, and $\Delta t_{1/4} = 0.3$. Let $C(S_i)$ and $C(\Delta t_i)$ denote the numerical solutions for the step sizes S_i and, respectively, Δt_i for $i \in \{1, 1/2, 1/4\}$. Then, the following relative errors were calculated [46]:

$$E_1 = \frac{\|C(S_1) - C(S_{1/4})\|}{\|C(S_{1/4})\|}, \; E_{1/2} = \frac{\|C(S_{1/2}) - C(S_{1/4})\|}{\|C(S_{1/4})\|},$$

and, respectively,

$$e_1 = \frac{\|C(\Delta t_1) - C(\Delta t_{1/4})\|}{\|C(\Delta t_{1/4})\|}, \; e_{1/2} = \frac{\|C(\Delta t_{1/2}) - C(\Delta t_{1/4})\|}{\|C(\Delta t_{1/4})\|},$$

where $\|\dot{\|}$ denotes the Frobenius norm. Lastly, the orders of convergence were also calculated as

$$p_S = \log_2\left(\frac{\|C(S_1) - C(S_{1/2})\|}{\|C(S_{1/2}) - C(S_{1/4})\|}\right), \; p_{\Delta t} = \log_2\left(\frac{\|C(\Delta t_1) - C(\Delta t_{1/2})\|}{\|C(\Delta t_{1/2}) - C(\Delta t_{1/4})\|}\right).$$

The results of these calculations are shown in Table 6. The combined space–time convergence and the time step size convergence are linear since $p_S \approx 1$, $p_{\Delta t} \approx 1$.

Table 6. Relative errors and orders of convergence for combined space–time convergence and time step size convergence, respectively.

Combined Space–Time	Time Step Size
$E_1 = 0.0719$	$e_1 = 0.003$
$E_{1/2} = 0.0266$	$e_{1/2} = 0.001$
$p_S = 1.1387 \approx 1$	$p_{\Delta t} = 1.001 \approx 1$

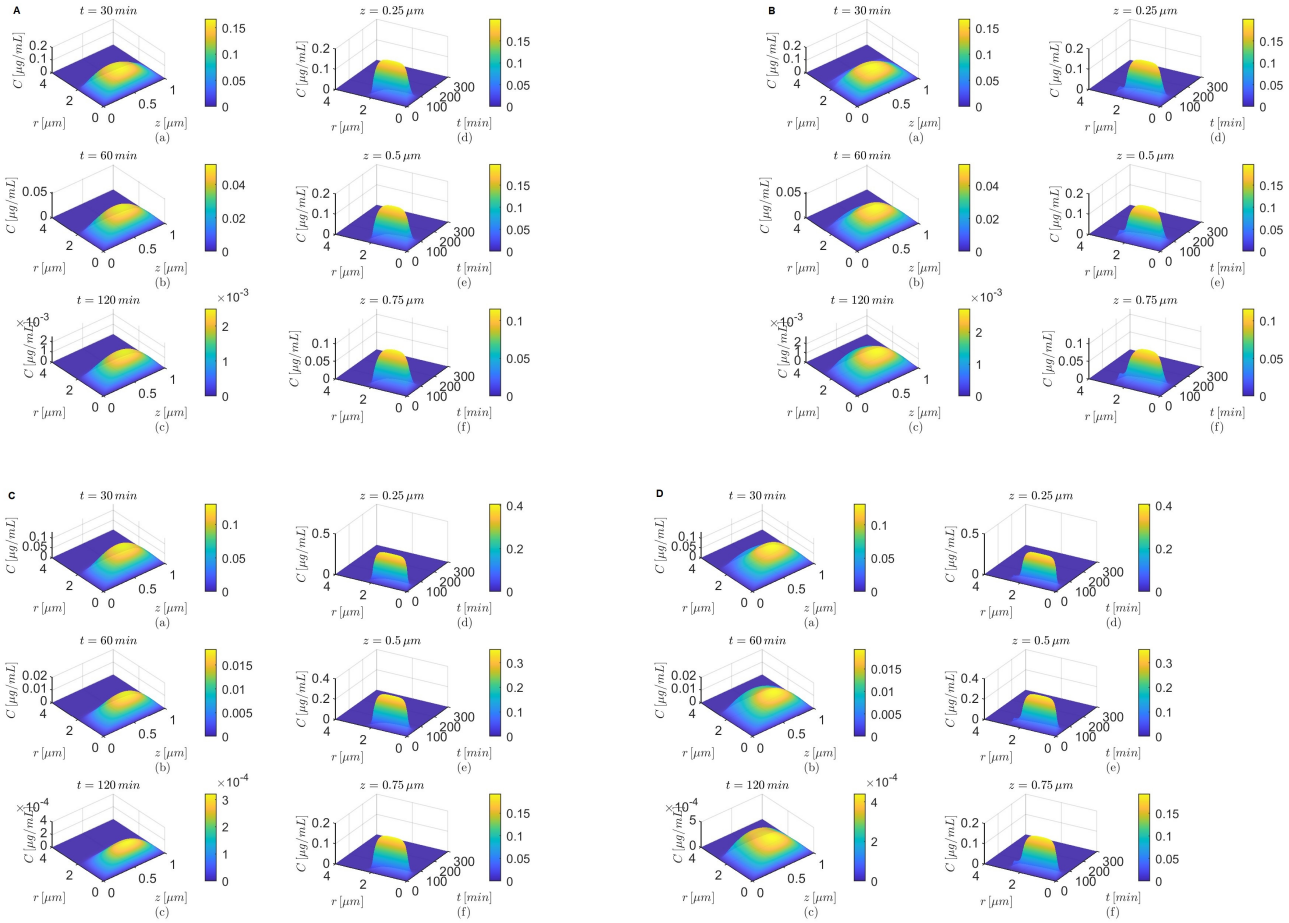

Figure 6. Results for $\varepsilon = 0.868$, $p_r = p_z = 0.5$, and $\alpha = 0$ (**A**,**B**) and $\alpha = 0.868$ (**C**,**D**) either in the absence (**A**,**C**) or in the presence (**B**,**D**) of the BBB transcytosis. Spatial variations in concentration C at three fixed times are shown in plots (**a**–**c**), and variations in C in time and along the radial direction at fixed locations along the capillary lumen are shown in plots (**d**–**f**).

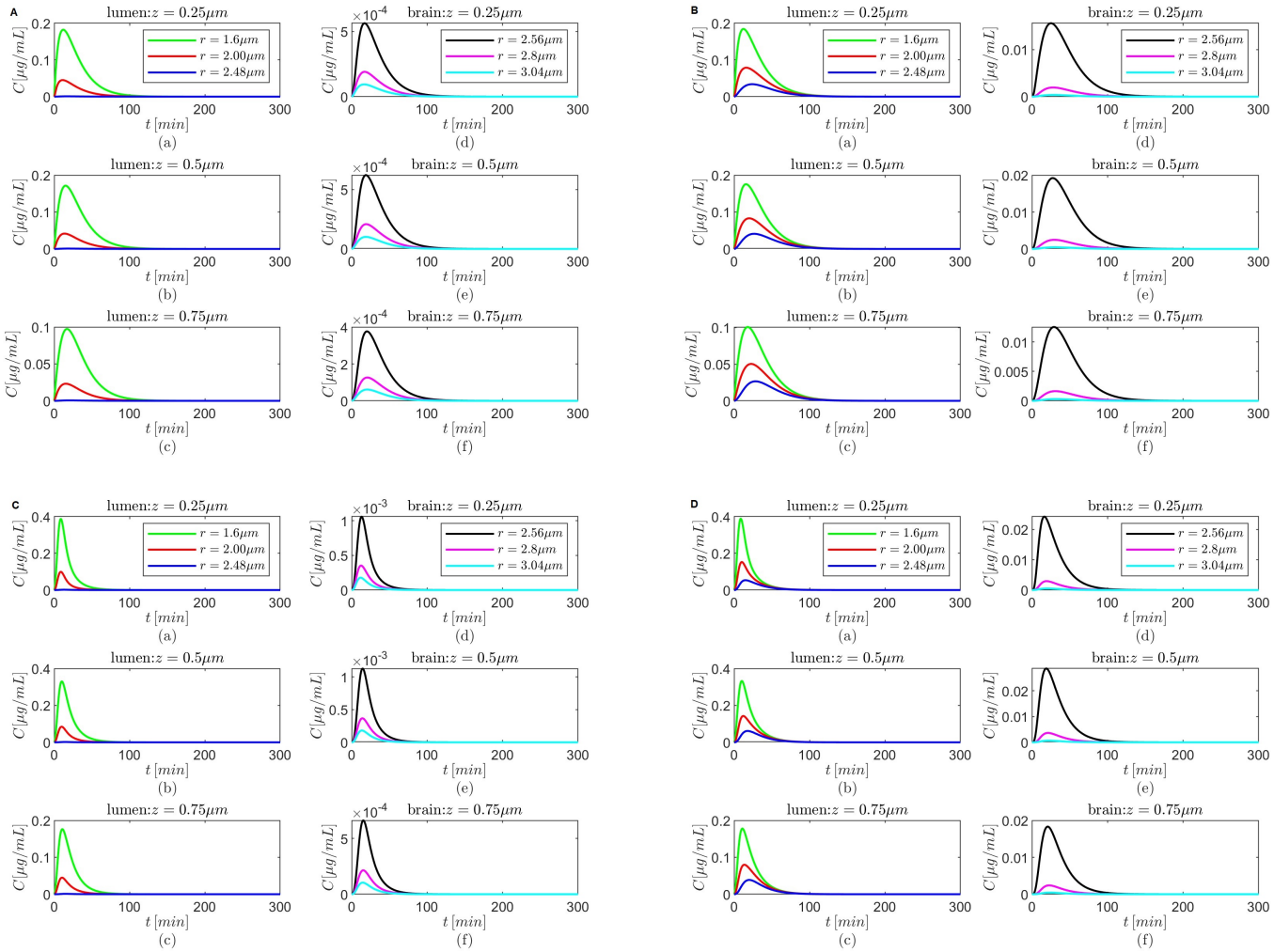

Figure 7. Results for $\varepsilon = 0.868$, $p_r = p_z = 0.5$, and $\alpha = 0$ (**A**,**B**) and $\alpha = 0.868$ (**C**,**D**) either in the absence (**A**,**C**) or in the presence (**B**,**D**) of the BBB transcytosis. Temporal variations in concentration C at various fixed locations in the capillary lumen (**a**–**c**) and brain parenchyma (**d**–**f**).

Using step sizes $S_{1/4}$ was computationally expensive even for one case, and therefore the step sizes $S_{1/2}$ were used instead.

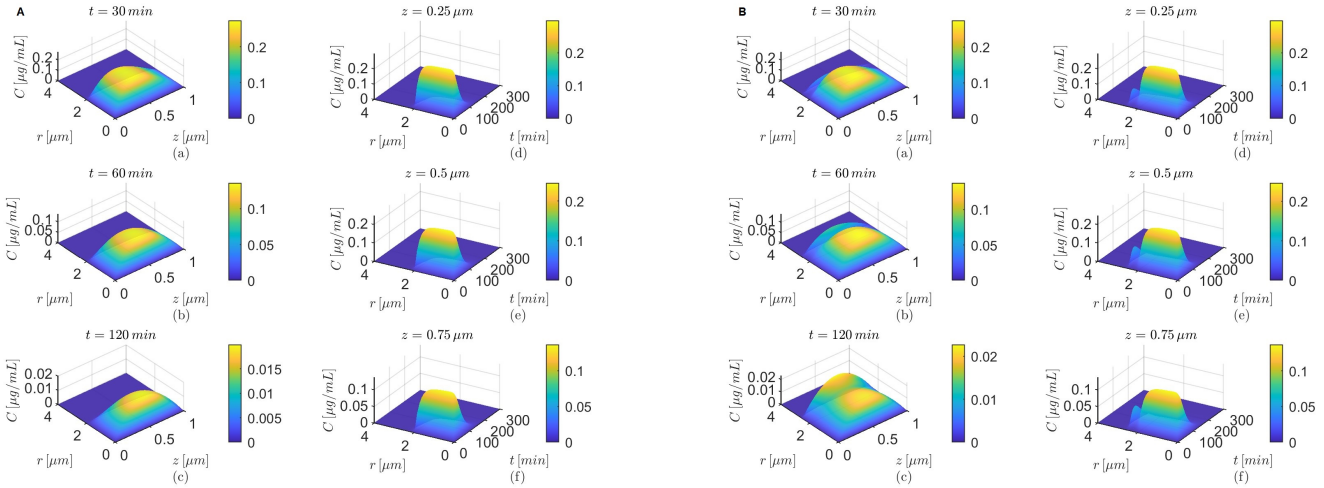

Figure 8. *Cont.*

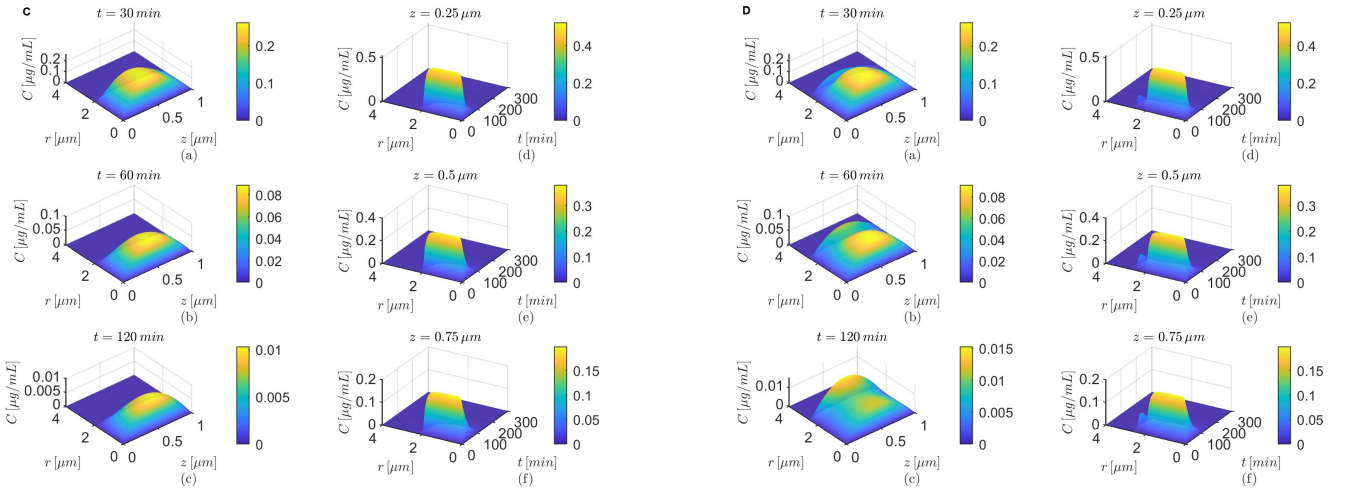

Figure 8. Results for $\varepsilon = 0.5$, $p_r = p_z = 0.5$, and $\alpha = 0$ (**A**,**B**) and $\alpha = 0.868$ (**C**,**D**) either in the absence (**A**,**C**) or in the presence (**B**,**D**) of the BBB transcytosis. Spatial variations in concentration C at three fixed times are shown in plots (**a**–**c**), and variations in C in time and along the radial direction at fixed locations along the capillary lumen are shown in plots (**d**–**f**).

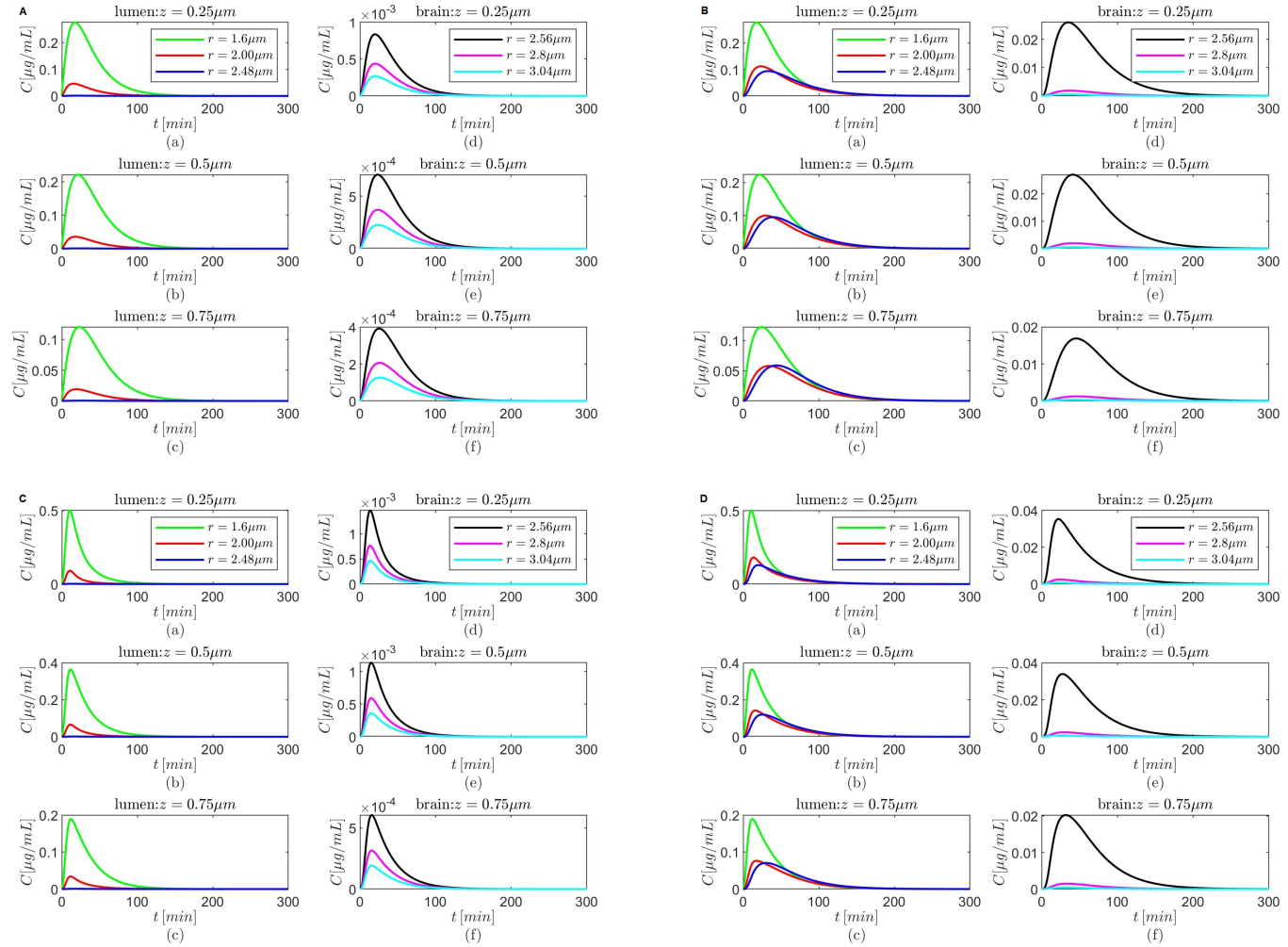

Figure 9. Results for $\varepsilon = 0.5$, $p_r = p_z = 0.5$, and $\alpha = 0$ (**A**,**B**) and $\alpha = 0.868$ (**C**,**D**) either in the absence (**A**,**C**) or in the presence (**B**,**D**) of the BBB transcytosis. Temporal variations in concentration C at various fixed locations in the capillary lumen (**a**–**c**) and brain parenchyma (**d**–**f**).

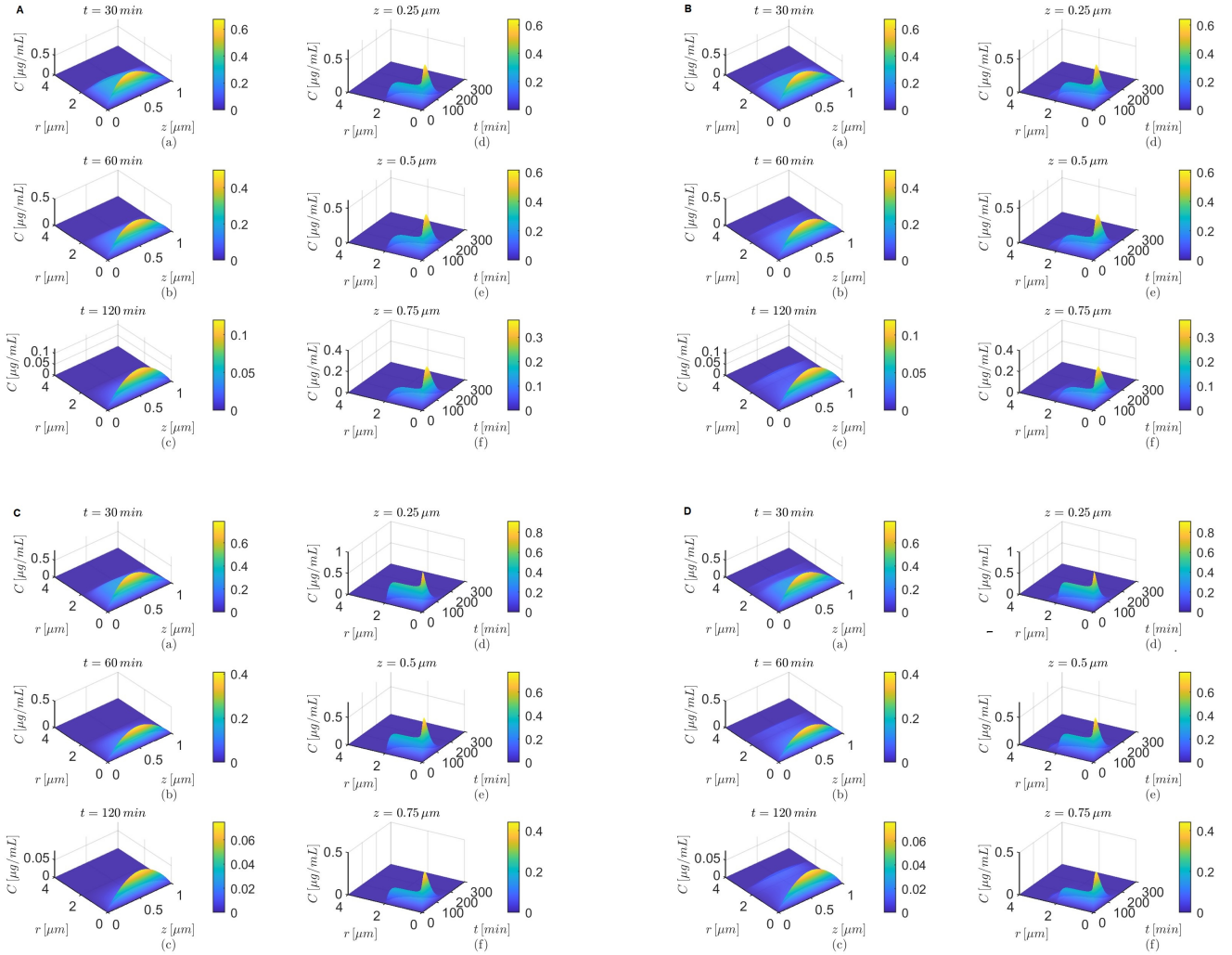

Figure 10. Results for $\varepsilon = 0.5$, $p_r = 1$, $p_z = 0.5$, and $\alpha = 0$ (**A**,**B**) and $\alpha = 0.868$ (**C**,**D**) either in the absence (**A**,**C**) or in the presence (**B**,**D**) of the BBB transcytosis. Spatial variations in concentration C at three fixed times are shown in plots (**a**–**c**), and variations in C in time and along the radial direction at fixed locations along the capillary lumen are shown in plots (**d**–**f**).

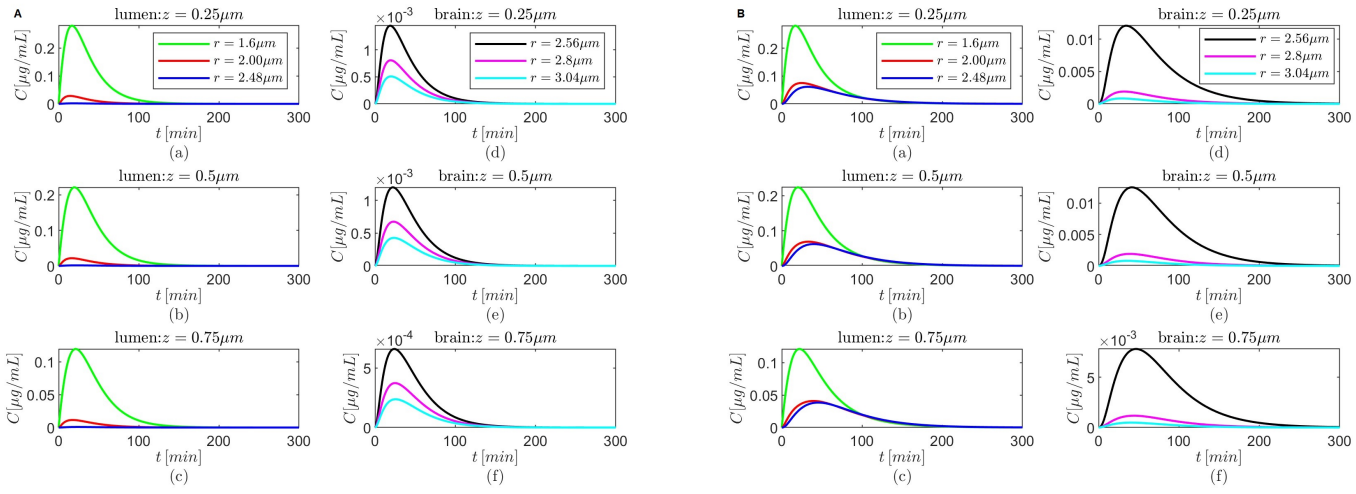

Figure 11. *Cont.*

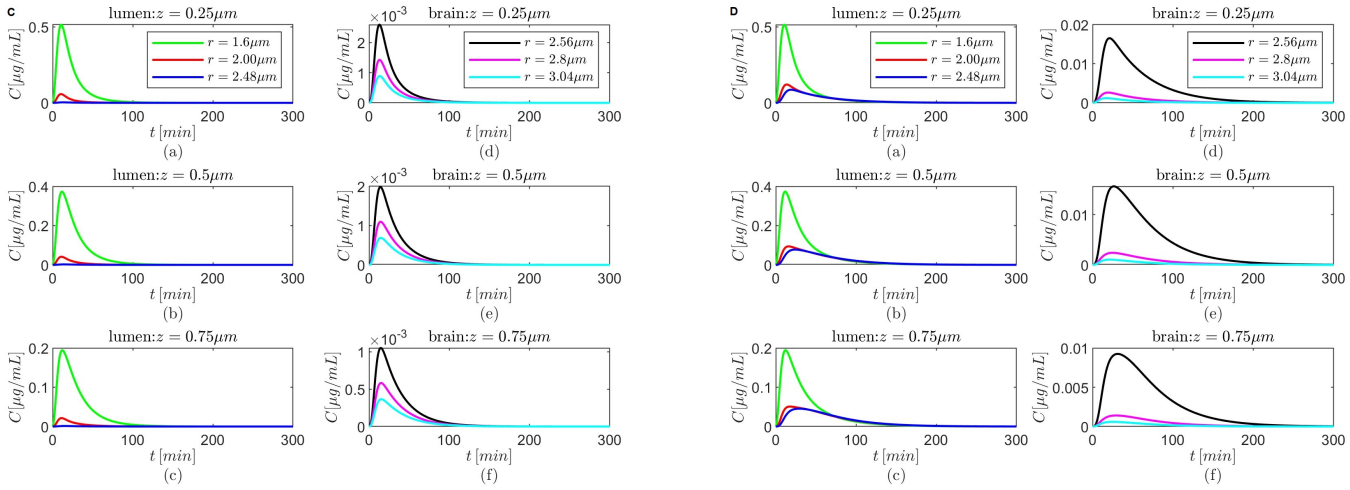

Figure 11. Results for $\varepsilon = 0.5$, $p_r = 1$, $p_z = 0.5$, and $\alpha = 0$ (**A**,**B**) and $\alpha = 0.868$ (**C**,**D**) either in the absence (**A**,**C**) or in the presence (**B**,**D**) of the BBB transcytosis. Temporal variations in concentration C at various fixed locations in the capillary lumen (**a**–**c**) and brain parenchyma (**d**–**f**).

4. Discussion

In this paper, a mathematical model of donepezil hydrochloride transport to a brain with AD after oral administration is proposed. The model assumes anomalous diffusion of the drug through a blood–brain region within the cerebral capillary bed and two scenarios: (1) the BBB transcytosis is present, and (2) the absence of the BBB transcytosis, describing the BBB disintegration seen in later stages of AD. The anomalous diffusion is due to the presence of structural damage and accumulation of harmful waste in the brain caused by AD and is modeled as Lévy flights characterized by self-similar clusters of local sojourns connected through long jumps [47]. Numerical simulations show that a functional BBB transcytosis can increase the drug's concentration deeper in the brain parenchyma, which supports ongoing pharmacological efforts [4,7,10]. Using the maximum drug concentrations at various locations in the brain parenchyma predicted by the model, the following drug delivery schemes tailored to AD severity emerge: 1) $\alpha = 0$, $\varepsilon = 0.868$, $p_r = p_z = 0.5$ or $\alpha = 0.868$, $\varepsilon = 1$, $p_r = p_z = 0.5$ for early stages of AD when the BBB transcytosis is still functional, and 2) $\alpha = 0$, $\varepsilon = 0.5$, $p_r = 1$, $p_z = 0.5$ or $\alpha = 0.868$, $\varepsilon = 0.5$, $p_r = 1$, $p_z = 0.5$ for late stages of AD when the BBB transcytosis is likely damaged. However, since the drug's clearance durations are shorter in the case where $\alpha = 0.868$ than in the case where $\alpha = 0$, the drug administration frequency will have to be higher for $\alpha = 0.868$ to obtain an effective treatment which, combined with the fact that the maximum drug concentrations are greater for $\alpha = 0.868$ than for $\alpha = 0$, may lead to increased adverse effects. Therefore, using $\alpha = 0$, $\varepsilon = 0.868$, $p_r = p_z = 0.5$ for early AD and $\alpha = 0$, $\varepsilon = 0.5$, $p_r = 1$, $p_z = 0.5$ for severe AD may be preferable. Since for a Lévy flight with index $\varepsilon + 1$, $0 < \varepsilon < 1$ its jump length probability density function decays asymptotically like a long-tailed inverse power-law function $\sigma^{1+\varepsilon}/|x|^{2+\varepsilon}$ (x stands for a generic spatial length), the jump length develops a longer tail as ε decreases. This means that treatment efficacy is achieved for either Lévy flights with index 1.868 combined with the BBB transcytosis (early stages of AD) or for Lévy flights with index 1.5 and radially outward skewness $p_r = 1$ when the BBB transcytosis is absent (late stages of AD).

These findings may inspire the development of novel brain-targeted drug delivery methods that may be useful for treating not only AD but also other brain diseases. In recent years, various strategies for using the BBB transcytosis and other mechanisms of BBB regulation and crossings have been developed for drug delivery to the brain [7,9–11,48–50]. For instance, some methods focus on the temporary and reversible opening of the BBB using optical, electrical, or mechanical stimulation [48]. While these are promising approaches for

treating certain brain diseases, they may be problematic for AD treatment for the following reasons: (1) the structural integrity and functionality of the BBB in a brain with AD are compromised and potentially more prone to damage from physical stimulation, (2) the opening of the BBB will allow for more $A\beta$ fibrils and other neurotoxins to enter the brain, thus intensifying AD progression, and (3) physical stimulation may damage astrocytes' endfeet, hindering their contributions to clearing waste and regulating neuroimmune responses [4,9]. Other drug delivery methods for brain targeting use nanocarriers with customized architectures and compositions that are engineered to control drug release by following a set of programmed protocols and/or by dynamically receiving and processing specific biochemical signals of the bodily structures (including the BBB) the carriers travel through [50]. These systems may be more suitable for AD treatment. For example, it was shown in [51] that a dual-functional nanoparticle drug delivery system for BBB transport and $A\beta$ targeting was able to successfully deliver a β-sheet breaker peptide to the brain in an AD mouse model. Also, ApoE-targeted and donepezil-loaded nanoparticles can use the binding of ApoE with BBB receptors to cross the BBB in a co-culture model of the BBB [18]. A comprehensive review of BBB-targeted drug delivery systems that could help with the AD treatment by increasing the $A\beta$ clearance across the BBB, recovering the structural intergrity and functionality of the BBB, or decreasing neuroinflammation is given in [9]. It is also worth mentioning the therapies used for BBB tissue repair after stroke reviewed in [52], since they may be relevant to the AD treatment of some patients. Neuroimaging and cerebrospinal fluid biomarkers could be used to assess not only the BBB disintegration with AD but also the BBB restoration after treatment [4].

Figure 12 shows a naive schematic for a multi (BBB and brain)-targeted drug delivery system that combines ligand functionalization, specialized coating, and information about the spatial distribution of relevant structures extracted from images of cerebral vasculature and the BBB [53,54] and brain ECS [55,56]. Lévy jumps could be practically achievable via a mixture of ligands attached to the drugs' molecules. The ligands have various lengths estimated from the above-mentioned images and different binding affinities. The lengths and binding strengths of the ligands relate to parameters ε and p_r, p_z, respectively, of the proposed model. This complex nanocarrier may be manufactured using 3D printing [57].

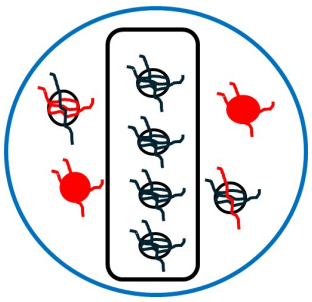

Figure 12. Naive schematic of a nanocarrier for combined BBB and neuronal targeting made of a layer protecting the digestive system (blue circle) and a layer able to cross the BBB via transcytosis (black rectangle) filled with donepezil molecules (black circles) with ligands (black lines) that bind to receptors of neurons near capillaries; donepezil molecules with mixed ligands that allow for BBB crossing (red lines) and binding to receptors of neurons near the BBB (black lines); and molecules of drugs preserving the BBB integrity (red circles with red ligands that bind to BBB-specific receptors).

One major challenge with the proposed model is finding the values of the physical parameters in vivo. The values of k_{12}, k_{20}, k_{23}, k_{30}, V_{blood}, and V_{brain} in Table 1 are taken from [24], where mice received donepezil solutions orally by gastrogavage and then the donepezil amounts were extracted from serum and brain tissue samples collected from the mice at specific time points. The process of collecting the samples involved the following steps: sacrificing the mice, collecting the blood by submandibular bleeding of mice followed by separating the serum by centrifugation, total body perfusion followed by brain dissection and homogenization, and extracting the donepezil amounts by vortexing the serum and

homogenized brain tissue samples. The data were analyzed and fitted to compartmental pharmacokinetic models using the software NONMEM 7.4 (NONlinear Mixed Effects Modeling). A three-compartment model that contains the above-mentioned parameters was found to best describe the data (for the sake of completeness, the equations of the model are given in Appendix A). In [23], a water-in-oil emulsion technique was used to prepare donepezil hydrochloride-encapsulated sodium alginate microspheres that can be administered orally. Studies of in vitro drug release from the microspheres were performed and the cumulative (temporal) release data were fitted to the power law (Ritger–Peppas) model. The drug release follows a Fickian diffusion pattern if the exponent of release is less than or equal to 0.5, and an anomalous (non-Fickian) diffusion pattern if the exponent of release is strictly greater than 0.5 and less than 1. The values of the exponents of release reported in [23] were assigned to the parameters α and ε (although the model proposed in this paper does not describe the experiments in [23], the only commonality between them is the anomalous diffusion aspect). Lastly, diffusion coefficients in the microspheres were also calculated in [23] using swelling experiments. Since diffusion coefficients of donepezil in the blood, BBB, and brain ECS are not reported in the literature even for Fickian transport, it is assumed that the generalized diffusion coefficient D takes one of the values of the diffusion coefficient for drug release reported in [23]. A parameter sensitivity analysis is beyond the scope of this paper because, at this stage of research, the focus is on the effects of the anomalous diffusion and BBB transcytosis on the spatio-temporal variations in the donepezil's concentration that are essential for the accurate delivery of drugs targeting neurons. The parameters taken from [24] were validated experimentally, so they will not be discussed further. Some comments on the diffusion coefficient will be given in the next paragraph.

Although the diffusion coefficient of a drug is a critical parameter that controls the availability and distribution of the drug in the body, there are relatively few published studies reporting diffusion coefficients of drugs because they are rather difficult to find experimentally. Various experimental modalities for measuring and formulas for calculating diffusion coefficients of nanoparticles in brain ECS were reviewed in [58] (see also a more recent review in [55]) and could potentially be used to find diffusion coefficients of nanoparticles in the blood and BBB in a brain with AD. According to [58], the effective diffusion coefficient $\tilde{D}^*$ of the brain ECS is

$$\tilde{D}^* = \frac{\tilde{D}_{\mathrm{w}}}{\lambda^2}, \tag{10}$$

where $\tilde{D}_{\mathrm{w}}$ is the classic free diffusion coefficient of nanoparticles diffusing through pure water and λ is the tortuosity of the ECS which, for a mouse model of AD, was found to be $\lambda = 1.52$ (Table 7 in [58]). The Stokes–Einstein equation may be used to calculate the classic diffusion coefficient $\tilde{D}$, but, according to [59], the equation may not be applicable to the orally administered solution used in [24] since the donepezil diameter in the solution is at most 100 nm while the equation is valid for diameters above 150 nm. However, for the nanoparticles containing donepezil used in [20], the Stokes–Einstein equation is valid since the average diameter of these nanoparticles is 270 nm. The Stokes–Einstein equation is as follows [60] (see also [58,59]):

$$\tilde{D} = \frac{k_B T}{3\pi\,\eta\,d_n}, \tag{11}$$

where $k_B = 1.38 \times 10^{-23}\,\mathrm{J\,K^{-1}}$ is the Boltzmann's constant; T is the temperature, which for the brain is $T = 37\ ^\circ\mathrm{C}$; η is the dynamic viscosity of the medium, which for pure water at 37 °C is $\eta = 0.69\,\mathrm{mPa\cdot s}$; and d_n is the diameter of the nanoparticle, which here is taken to be $d_n = 270$ nm. Performing the calculations in Formulas (11) and (10) gives $\tilde{D}_{\mathrm{w}} = 146\,\mu\mathrm{m}^2/\mathrm{min}$ and $\tilde{D}^* = 63.2\,\mu\mathrm{m}^2/\mathrm{min}$. Also, the dynamic viscosity of blood at 37 °C is $\eta = 2.78\,\mathrm{mPa\cdot s}$ [61], which is within the range for viscosities for which the Stokes–Einstein equation is valid [59]. Thus, the diffusion coefficient of the nanoparticles in [20] diffusing through blood can be calculated using the Stokes–Einstein Equation (11) and

has the value $\tilde{D}_{\text{blood}} = 36.2\,\mu\text{m}^2/\text{min}$. These calculations show not only that the classic diffusion coefficients of nanoparticles with donepezil in the blood and brain ECS could be orders of magnitude higher than the diffusion coefficients of donepezil in carriers reported in [23] but also that these diffusion coefficients may not have the same value. It is very likely that these observations on the classic diffusion coefficients will remain valid for the generalized diffusion coefficients of donepezil. If the diffusion coefficient in Table 1 is increased by a factor 10^4 (so its value is approximately equal to $\tilde{D}^*$), then the drug's concentrations predicted by the proposed model decrease by a factor of about 10^3. The model does not work for a non-constant generalized diffusion coefficient. Lastly, it is worth mentioning the work in [62], where the diffusion coefficients of some drugs in an unstirred aqueous environment were found using data obtained by UV visible spectroscopy which were fitted to the classic diffusion equation. By tailoring the cuvette geometry so that it looks like the capillary lumen, the BB,B and the brain ECS [53–56] and using the approach in [62], the data could be fitted to the one-dimensional form of the non-local diffusion Equation (2) (without the sink and source terms) to find the generalized diffusion coefficients D of donepezil in the regions of interest (capillary lumen, the BBB, and the brain ECS) and corresponding parameters ε. The model will have to be adjusted to properly account for non-constant values of D and ε not only in different regions but also along different directions. Ultimately, variable-order fractional operators may have to replace the constant-order fractional derivatives used in Formula (3) since some studies showed that anomalous diffusion through an inhomogeneous porous medium or a medium with predefined diffusion patterns is not well described by constant-order fractional operators [63]. To account for other AD-specific processes, such as neuroinflammation dynamics and the growth of the $A\beta$ plaques, the model's parameters, which are currently constants, could become functions of physical quantities predicted by other models and new coupling terms could be added to the equations of the considered models.

Presently, there are no published studies that could be used to validate the proposed model. Spatial averages over the blood and brain regions of the donepezil concentrations predicted by the model cannot be compared to the experimental data in [24] since the model considers a small brain region near one cerebral capillary, while the donepezil amounts in [24] were estimated from whole blood and (homogenized and fixed) brain tissue volumes. Hopefully, this work will inspire new studies of transport to the brain of donepezil or other brain-targeted drugs that will measure drug concentrations not only at various time points but also at different locations in a brain.

5. Conclusions

In this paper, a mathematical model of the AD drug donepezil hydrochloride's transport to the brain after oral administration is proposed. The model describes the anomalous diffusion of the drug through a blood–brain region within the cerebral capillary bed, and either a functional BBB transcytosis for earlier stages of AD or the absence of the BBB transcytosis for later stages of AD. The anomalous diffusion is modeled as Lévy flights with index $\varepsilon + 1$, $0 < \varepsilon < 1$ and represented mathematically by spatial Riemann–Liouville fractional derivatives of order ε. Numerical simulations suggest that, to obtain a better treatment, the drug delivery and release modalities should depend on the BBB transcytosis functionality and anomalous diffusion and be tailored to the AD severity. These results may inspire new drug nanocarriers for improved AD treatments.

Funding: This research received no external funding.

Institutional Review Board Statement: Not applicable.

Informed Consent Statement: Not applicable.

Data Availability Statement: The original contributions presented in the study are included in the article, further inquiries can be directed to the corresponding author.

Conflicts of Interest: The authors declare no conflict of interest. The funders had no role in the design of the study; in the collection, analyses, or interpretation of data; in the writing of the manuscript, or in the decision to publish the results.

Abbreviations

The following abbreviations are used in this manuscript:

AD	Alzheimer's Disease
BBB	Blood–Brain Barrier
ECS	Extracellular Space
ISF	Interstitial Fluid

Appendix A

In [24], the compartmental pharmacokinetic modeling and fitting to experimental data were performed using the software NONMEM 7.4 and, therefore, the equations of the population models that describe best the data were not given. To make the presentation comprehensive and highlight the original contributions of this paper, the equations of the three-compartment model described in [24] are presented further.

$$\begin{aligned}
\dot{c}_d(t) &= -k_{12}\, c_d(t) \\
\dot{c}_{\text{blood}}(t) &= k_{12}\, c_d(t) - (k_{20} + k_{23} + k_{24})\, c_{\text{blood}}(t) + k_{42}\, c_p(t) \\
\dot{c}_{\text{brain}}(t) &= \frac{V_{\text{blood}}}{V_{\text{brain}}}\, k_{23}\, c_{\text{blood}}(t) - k_{30}\, c_{\text{brain}}(t) \\
\dot{c}_p(t) &= k_{24}\, c_{\text{blood}}(t) - k_{42}\, c_p(t),
\end{aligned}$$

where the symbol $\dot{}$ denotes the first-order temporal derivative, and c_d, c_{blood}, c_{brain}, and c_p are the drug's concentrations in the depot, blood, brain, and peripheral compartments, respectively. Since the system is linear, an exact solution can be found:

$$\begin{pmatrix} c_d \\ c_{\text{blood}} \\ c_{\text{brain}} \\ c_p \end{pmatrix} = \sum_{i=1}^{4} c_i\, \mathbf{v}_i\, \exp(\lambda_i\, t),$$

where λ_i, $i \in \{1,2,3,4\}$ are the eigenvalues of the system's matrix, $\mathbf{v}_i$, $i \in \{1,2,3,4\}$ are the corresponding eigenvectors, and c_i, $i \in \{1,2,3,4\}$ are constants of integration.

References

1. Carreiras, M.C.; Mendes, E.; Perry, M.J.; Francisco, A.P.; Marco-Contelles, J. The multifactorial nature of Alzheimer's disease for developing potential therapeutics. *Curr. Top. Med. Chem.* **2013**, *13*, 1745–1770. [CrossRef] [PubMed]
2. World Health Organization. Dementia Key Facts. Available online: https://www.who.int/news-room/fact-sheets/detail/dementia (accessed on 20 July 2024).
3. Alzheimer, A. Uber einen eigenartigen schweren Erkrankungsprozess der Hirninde. *Neurol. Centralblatt.* **1906**, *25*, 1134.
4. Sweeney, M.D.; Sagare, A.P.; Zlokovic, B.V. Blood–brain barrier breakdown in Alzheimer disease and other neurodegenerative disorders. *Nat. Rev. Neurol.* **2018**, *14*, 133–150. [PubMed]
5. Salman, M.M.; Kitchen, P.; Halsey, A.; Wang, M.X.; Törnroth-Horsefield, S.; Conner, A.C.; Badaut, J.; Iliff, J.J.; Bill, R.M. Emerging roles for dynamic aquaporin-4 subcellular relocalization in CNS water homeostasis. *Brain* **2022**, *145*, 64–75. [CrossRef]
6. Kinney, J.W.; Bemiller, S.M.; Murtishaw, A.S.; Leisgang, A.M.; Salazar, A.M.; Lamb, B.T. Inflammation as a central mechanism in Alzheimer's disease. *Alzheimer's Dement. Transl. Res. Clin. Interv.* **2018**, *4*, 575–590. [CrossRef]
7. Wu, D.; Chen, Q.; Chen, X.; Han, F.; Chen, Z.; Wang, Y. The blood-brain barrier: Structure, regulation, and drug delivery. *Signal Transduct. Target. Ther.* **2023**, *8*, 217. [CrossRef]
8. Montagne, A.; Zhen Zhao, Z.; Zlokovic, B.V. Alzheimer's disease: A matter of blood–brain barrier dysfunction? *J. Exp. Med.* **2017**, *214*, 3151–3169. [CrossRef]
9. Alkhalifa, A.E.; Al-Ghraiybah, N.F.; Odum, J.; Shunnarah, J.G.; Austin, N.; Kaddoumi, A. Blood–brain barrier breakdown in Alzheimer's disease: Mechanisms and targeted strategies. *Int. J. Mol. Sci.* **2023**, *24*, 16288. [CrossRef]

10. Pulgar, V.M. Transcytosis to cross the blood brain barrier, new advancements and challenges. *Front. Neurosci.* **2019**, *12*, 1019. [CrossRef]
11. Choudhari, M.; Hejmady, S.; Saha, R.N.; Damle, S.; Singhvi, G.; Alexander, A.; Kesharwani, P.; Dubey, S.K. Evolving new-age strategies to transport therapeutics across the blood-brain-barrier. *Int. J. Pharm.* **2021**, *599*, 120351. [CrossRef]
12. Mader, S.; Brimberg, L. Aquaporin-4 water channel in the brain and its implication for health and disease. *Cells* **2019**, *8*, 90. [CrossRef] [PubMed]
13. Kumar, A.; Gupta, V.; Sharma, S. Donepezil. [Updated 2023 Aug 17]. In *StatPearls [Internet]*; StatPearls Publishing: Treasure Island, FL, USA, 2024. Available online: https://www.ncbi.nlm.nih.gov/books/NBK513257/ (accessed on 20 July 2024).
14. Sam, C.; Bordoni, B. Physiology, Acetylcholine. [Updated 2023 Apr 10]. In *StatPearls [Internet]*; StatPearls Publishing: Treasure Island, FL, USA, 2024. Available online: https://www.ncbi.nlm.nih.gov/books/NBK557825/ (accessed on 16 August 2024).
15. Kim, J.; Lee, H.J.; Park, S.K.; Park, J.H.; Jeong, H.R.; Lee, S.; Lee, H.; Seol, E.; Hoe, H.S. Donepezil regulates LPS and *Aβ*-stimulated neuroinflammation through MAPK/NLRP3 inflammasome/STAT3 signaling. *Int. J. Mol. Sci.* **2021**, *22*, 10637. [CrossRef] [PubMed]
16. Jakki, S.L.; Ramesh, Y.V.; Gowthamarajan, K.; Senthil, V.; Jain, K.; Sood, S.; Pathak, D. Novel anionic polymer as a carrier for CNS delivery of anti-Alzheimer drug. *Drug Deliv.* **2016**, *23*, 3471–3479. [CrossRef]
17. Silva, R.O.; Counil, H.; Rabanel, J.-M.; Haddad, M.; Zaouter, C.; Khedher, M.R.B.; Patten, S.A.; Ramassamy, C. Donepezil-loaded nanocarriers for the treatment of Alzheimer's disease: Superior efficacy of extracellular vesicles over polymeric nanoparticles. *Int. J. Nanomed.* **2024**, *19*, 1077–1096. [CrossRef] [PubMed]
18. Topal, G.R.; Mészáros, M.; Porkoláb, G.; Szecskó, A.; Polgár, T.F.; Siklós, L.; Deli, M.A.; Veszelka, S.; Bozkir, A. ApoE-targeting increases the transfer of solid lipid nanoparticles with donepezil cargo across a culture model of the blood–brain barrier. *Pharmaceutics* **2021**, *13*, 38. [CrossRef] [PubMed]
19. Topal, G.R.; Kücüktürkmen, B.; Öz, U.C.; Özkan, E.; Bakar-Ates, F.; Bozkir, A. Investigation on formulation parameters of donepezil HCl loaded solid lipid nanoparticles. *Braz. J. Pharm. Sci.* **2023**, *59*, e22330. [CrossRef]
20. Tao, X.; Mao, S.; Zhang, Q.; Yu, H.; Li, Y.; He, X.; Yang, S.; Zhang, Z.; Yi, Z.; Song, Y.; et al. Brain-targeted polysorbate 80-emulsified donepezil drug-loaded nanoparticles for neuroprotection. *Nanoscale Res. Lett.* **2021**, *16*, 132. [CrossRef]
21. Akyol, E.; Senol, S.; Dogan, Ö. Controlled release of donepezil hydrochloride from the ternary sodium alginate based hydrogels. *Bulg. Chem. Commun.* **2017**, *49*, 57–63.
22. Ruela, A.L.; Carvalho, F.C.; Pereira, G.R. Exploring the phase behavior of monoolein/oleic acid/water Systems for enhanced donezepil administration for Alzheimer disease treatment. *J. Pharm. Sci.* **2016**, *105*, 71–77. [CrossRef]
23. Bulut, E.; Sanli, O. Delivery of Alzheimer's drug donepezil hydrochloride from ionically crosslinked alginate microspheres prepared by water-in-oil emulsion technique: Optimization of release conditions. *Asian J. Chem.* **2013**, *25*, 3993–4000. [CrossRef]
24. Kaikousidis, C.; Papakyriakopoulou, P.; Dokoumetzidis, A.; Valsami, G. Donepezil brain and blood pharmacokinetic modeling after nasal film and oral solution administration in mice. *Pharmaceutics* **2023**, *15*, 1409. [CrossRef] [PubMed]
25. Papakyriakopoulou, P.; Balafas, E.; Colombo, G.; Rekkas, D.M.; Kostomitsopoulos, N.; Valsami, G. Nose-to-brain delivery of donepezil hydrochloride following administration of an HPMC-Me-β-CD-PEG400 nasal film in mice. *J. Drug Deliv. Sci. Technol.* **2023**, *84*, 104463. [CrossRef]
26. Espinoza, L.C.; Guaya, D.; Calpena, A.C.; Perotti, R.M.; Halbaut, L.; Sosa, L.; Brito-Llera, A.; Mallandrich, M. Comparative study of donepezil-loaded formulations for the treatment of Alzheimer's disease by nasal administration. *Gels* **2022**, *8*, 715. [CrossRef] [PubMed]
27. Zhang, P.; Chen, L.; Gu, W.; Xu, Z.; Gao, Y.; Li, Y. In vitro and in vivo evaluation of donepezil-sustained release microparticles for the treatment of Alzheimer's disease. *Biomaterials* **2007**, *28*, 1882–1888. [CrossRef]
28. Kearney, M.-C.; Caffarel-Salvador, E.; Fallows, S.J.; Helen, O. McCarthy, H.O.; Ryan F. Donnelly, R.F. Microneedle-mediated delivery of donepezil: Potential for improved treatment options in Alzheimer's disease. *Eur. J. Pharm. Biopharm.* **2016**, *103*, 43–50. [CrossRef]
29. Siepmann, J.; Siepmann, F. Modeling of diffusion controlled drug delivery. *J. Control. Release* **2012**, *161*, 351–362 [CrossRef] [PubMed]
30. Bruschi, M.L. *Strategies to Modify the Drug Release from Pharmaceutical Systems*; Woodhead Publishing: Cambridge, UK, 2015; pp. 63–86.
31. Trucillo, P. Drug carriers: A review on the most used mathematical models for drug release. *Processes* **2022**, *10*, 1094. [CrossRef]
32. Khanday, M.A.; Rafiq, A.; Nazir, K. Mathematical models for drug diffusion through the compartments of blood and tissue medium. *Alex. J. Med.* **2017**, *53*, 245–249.
33. Shyamsunder, S.; Bhatter, K.J.; Purohit, S.D. Fractionalized mathematical models for drug diffusion. *Chaos Solitons Fractals* **2022**, *165*, 112810. [CrossRef]
34. Alijani, Z.; Shiri, B.; Perfilieva, I.; Baleanu, D. Numerical solution of a new mathematical model for intravenous drug administration. *Evol. Intell.* **2024**, *17*, 559–575. [CrossRef]
35. Rudin, W. *Real and Complex Analysis*, 3rd ed.; McGraw-Hill Book Company: New York, NY, USA, 1987; pp. 144–147.
36. Samko, S.G.; Kilbas, A.A.; Marichev, O.I. *Fractional Integrals and Derivatives Theory and Applications*, 1st ed.; Gordon and Breach Science Publishers: London, UK, 1993; pp. 32–36.
37. Venetis, J. An analytic exact form of the unit step function. *Math. Stat.* **2014**, *2*, 235–237. [CrossRef]

38. Bracko, O.; Njiru, B.N.; Swallow, M.; Ali, M.; Haft-Javaherian, M.; Schaffer, C.B. Increasing cerebral blood flow improves cognition into late stages in Alzheimer's disease mice. *J. Cereb. Blood Flow Metab.* **2020**, *40*, 1441–1452. [CrossRef] [PubMed]
39. Steinman, J.; Sun, H.-S.; Feng, Z.-P. Microvascular alterations in Alzheimer's disease. *Front. Cell. Neurosci.* **2021**, *14*, 618986. [CrossRef]
40. Kim, S.; Kavvas, M.L. Generalized Fick's law and fractional ADE for pollution transport in a river: Detailed derivation. *J. Hydrol. Eng.* **2006**, *11*, 80–83. [CrossRef]
41. *MATLAB R2024a*; The MathWorks, Inc.: Natick, MA, USA, 2024.
42. Sousa, E. Finite difference approximations for a fractional advection diffusion problem. *J. Comput. Phys.* **2009**, *228*, 4038–4054. [CrossRef]
43. Müller, B.; Lang, S.; Dominietto, M.; Rudin, M.; Schulz, G.; Deyhle, H.; Germann, M.; Pfeiffer, F.; David, C.; Weitkamp, T. High-resolution tomographic imaging of microvessels. In Proceedings of the SPIE, San Diego, CA, USA, 10–14 August 2008; Volume 7078.
44. Tsai, P.S.; Kaufhold, J.P.; Blinder, P.; Friedman, B.; Drew, P.J.; Karten, H.J.; Lyden, P.D.; Kleinfeld, D. Correlations of neuronal and microvascular densities in murine cortex revealed by direct counting and colocalization of nuclei and vessels. *J. Neurosci.* **2009**, *29*, 14553–14570. [CrossRef]
45. Kaya, M.; Ahishali, B. Basic physiology of the blood-brain barrier in health and disease: A brief overview. *Tissue Barriers* **2021**, *9*, e1840913. [CrossRef] [PubMed]
46. LeVeque, R.J. *Finite Difference Methods for Ordinary and Partial Differential Equations: Steady-State and Time-Dependent Problems*, 1st ed.; Society for Industrial and Applied Mathematics: Philadelphia, PA, USA, 2007; pp. 254–258.
47. Metzler, R.; Klafter, J. The restaurant at the end of the random walk: Recent developments in the description of anomalous transport by fractional dynamics. *J. Phys. A Math. Gen.* **2004**, *37*, R161. [CrossRef]
48. Stamp, M.E.M.; Halwes, M.; Nisbet, D.; Collins, D.J. Breaking barriers: Exploring mechanisms behind opening the blood-brain barrier. *Fluids Barriers CNS* **2023**, *20*, 87. [CrossRef]
49. Garcia-Chica, J.; Paraiso, W.K.D.; Tanabe, S.; Serra, D.; Herrero, L.; Casals, N.; Garcia, J.; Ariza, X.; Quader, S.; Rodriguez-Rodriguez, R. An overview of nanomedicines for neuron targeting. *Nanomedicine* **2020**, *15*, 1617–1636. [CrossRef]
50. Moreira, R.; Nóbrega, C.; de Almeida, L.P.; Mendonça, L. Brain-targeted drug delivery—Nanovesicles directed to specific brain cells by brain-targeting ligands. *J. Nanobiotechnol.* **2024**, *22*, 260. [CrossRef] [PubMed]
51. Zhang, C.; Zheng, X.; Wan, X.; Shao, X.; Liu, Q.; Zhang, Z.; Zhang, Q. The potential use of H102 peptide-loaded dual-functional nanoparticles in the treatment of Alzheimer's disease. *J. Control. Release* **2014**, *192*, 317–324. [CrossRef]
52. Qi, L.; Wang, F.; Sun, X.; Li, H.; Zhang, K.; Li, J. Recent advances in tissue repair of the blood-brain barrier after stroke. *J. Tissue Eng.* **2024**, *15*, 20417314241226551. [CrossRef]
53. Weller, R.O.; Boche, D.; Nicoll, J.A.R. Microvasculature changes and cerebral amyloid angiopathy in Alzheimer's disease and their potential impact on therapy. *Acta Neuropathol.* **2009**, *118*, 87–102. [CrossRef] [PubMed]
54. Ando, Y.; Okada, H.; Takemura, G.; Suzuki, K.; Takada, C.; Tomita, H.; Zaikokuji, R.; Hotta, Y.; Miyazaki, N.; Yano, H.; et al. Brain-specific ultrastructure of capillary endothelial glycocalyx and its possible contribution for blood brain barrier. *Sci. Rep.* **2018**, *8*, 17523. [CrossRef]
55. Soria, F.N.; Miguelez, C.; Peñagarikano, O.; Tonnesen, J. Current techniques for investigating the brain ECS. *Front. Neurosci.* **2020**, *14*, 570750. [CrossRef]
56. Song, K.; Feng, Z.; Helmstaedter, M. High-contrast en bloc staining of mouse whole-brain and human brain samples for EM-based connectomics. *Nat. Methods* **2023**, *20*, 836–840. [CrossRef]
57. Jain, K.; Shukla, R.; Yadav, A.; Ujjwal, R.R.; Flora, S.J.S. 3D printing in development of nanomedicines. *Nanomaterials* **2021**, *11*, 420. [CrossRef]
58. Syková, E.; Nicholson, C. Diffusion in brain extracellular space. *Physiol. Rev.* **2008**, *88*, 1277–1340. [CrossRef]
59. Coglitore, D.; Edwardson, S.P.; Macko, P.; Patterson, E.A.; Whelan, M. Transition from fractional to classical Stokes–Einstein behaviour in simple fluids. *R. Soc. Open Sci.* **2017**, *4*, 170507. [CrossRef]
60. Sutherland, W. A dynamical theory of diffusion for non-electrolytes and the molecular mass of albumin. *Philos. Mag.* **1905**, *9*, 49–54. [CrossRef]
61. Viscosity of Whole Blood. Available online: https://wiki.anton-paar.com/us-en/whole-blood/ (accessed on 20 July 2024).
62. Pio di Cagno, M.; Clarelli, F.; Våbenø, J.; Lesley, C.; Rahman, S.D.; Cauzzo, J.; Franceschinis, E.; Realdon, N.; Stein, P.C. Experimental determination of drug diffusion coefficients in unstirred aqueous environments by temporally resolved concentration measurements. *Mol. Pharm.* **2018**, *15*, 1488–1494. [CrossRef] [PubMed]
63. Atangana, A.; Secer, A. A note on fractional order derivatives and table of fractional derivatives of some special functions. *Abstr. Appl. Anal.* **2013**, *2013*, 279681. [CrossRef]